Assessment of Tissue Micro-structure with Diffusion Weighted Magnetic Resonance Imaging

Inauguraldissertation

zur Erlangung der Würde eines Doktors der Philosophie
vorgelegt der
Philosophisch-Naturwissenschaftlichen Fakultät
der Universität Basel

von
Jinxia Zhu
aus Liaoning, China

UNI
BASEL

Basel, 2013

Genehmigt von der Philosophisch-Naturwissenschaftlichen Fakultät

auf Antrag von:

Prof. Dr. Klaus Scheffler
Referent
Prof. Dr. Michael Bock
Korreferent

Basel, den 12.11.2013

Prof. Dr. Jörg Schibler
Dekan

Abstract

Based on the pioneer works of Hahn in 1950, Carr and Purcell in 1954, and Stejskal and Tanner in the 1960s, Le Bihan and Breton introduced diffusion weighted imaging (DWI) technique in 1985. Then in 1986, Le Bihan presented the first DWI images of the human brain. From then on, DWI has become a very important area of MRI research.

Measurements of tissue microstructure can be very important in both clinical and research application. DWI is dependent on specific microstructural properties of biological tissues, so it is possible to obtain structural information non-invasively from DWI measurements. Diffusion in tissues is slower than in free solutions because tissue compartments hinder or restrict fluid motions, and the reduction in diffusion rate reflects the scale and nature of the tissue environment. Although DWI is becoming a mature method, there are still problems with the validation of this technique needed to be solved.

The first part of this PhD dissertation compares several sequences for the visualization of facial skeletal muscle with diffusion tensor imaging (DTI), which enables the investigation of micro-architecture and connectivity of oriented tissues. Readout segmented echo planar imaging (RS-EPI) has been suggested as an alternative to single-shot EPI (SS-EPI) for DWI with reduced distortion, which shows more reliable facial muscle fiber tracts. While diffusion weighted double echo steady state free precession sequence (DW-DESS) is relaxation independent, with higher resolution and considerably higher SNR . By using this approach, the image can achieve a higher resolution, giving more information of the small facial muscle groups.

The second part of this thesis refers to comparison of different diffusion models in renal diffusion imaging. The aim is to obtain additional parameters with stretched-

exponential, bi-exponential and kurtosis analysis of multiple b-value DWI and compare these parameters to apparent diffusion coefficient (ADC) obtained with mono-exponential model in their ability to discriminate different tumor types.

Contents

1 Outline **9**

2 Basic Principles of Magnetic Resonance Imaging **13**

- 2.1 Introduction 15
- 2.2 Magnetization 16
- 2.3 Three Magnetic Fields 17
- 2.4 Bloch equations 19
  - 2.4.1 Precession 19
  - 2.4.2 Excitation 19
  - 2.4.3 Relaxation 22
    - 2.4.3.1 T_1: Longitudinal Relaxation or spins-lattice relaxation . 22
    - 2.4.3.2 T_2 / T_2^*: Transverse Relaxation or spin-spin relaxation . 24
  - 2.4.4 Full Bloch equation with relaxation 26
- 2.5 Spatial encoding and k-space 27
  - 2.5.1 Magnetic field gradients for imaging 27
    - 2.5.1.1 Slice selection 27
    - 2.5.1.2 Frequency Encoding 29
    - 2.5.1.3 Phase Encoding 29
  - 2.5.2 An example: Gradient Echo Imaging 30
  - 2.5.3 K-space 31
- 2.6 Image contrast 33

References **35**

- References 35

3 Diffusion MRI theory **37**

- 3.1 Physics of Diffusion 39

3.1.1 Free diffusion 39
3.1.2 Restricted Diffusion 40
3.2 Diffusion weighting 41
3.2.1 Diffusion weighted imaging with Spin Echoes 41
3.2.2 Diffusion MR Imaging with Echo Planar Imaging Techniques (EPI) 43
3.2.2.1 Diffusion MR Imaging with single shot EPI 43
3.2.2.2 Diffusion MR Imaging with Multi-shot Interleaved EPI 44
3.2.2.3 Diffusion MR Imaging with Multi-shot Readout-Segmented EPI 45
3.2.3 Diffusion MR Imaging with Steady-State Free Precession (SSFP) 47
3.2.3.1 Steady-State Free Precession (SSFP) 48
3.2.3.2 Steady-State diffusion weighted imaging 48
3.2.3.3 Diffusion weighted Double Echo Steady-State Free Precession (DW-DESS) 49
3.3 Models 51
3.3.1 The Mono-exponential Model: Apparent diffusion coefficient ADC 51
3.3.2 The Bi-exponential Model: intravoxel incoherent motion (IVIM) 51
3.3.3 The Stretched-exponential Model 53
3.3.4 The Kurtosis Model 54
3.4 Diffusion Tensor Imaging 56
3.4.1 Diffusion Anisotropy 56
3.4.2 Diffusion Tensor 56
3.4.3 Diffusion Tensor Imaging (DTI) 58
3.4.4 DTI Fiber Tractography 59

References 61

References 61

4 Assessment of structural properties of facial skeletal muscle with diffusion MRI 67

4.1 Introduction 69
4.2 Materials and Methods 71
4.2.1 Imaging Techniques 71
4.2.2 Image Acquisition 72
4.2.3 Data Processing and Visualization 73
4.3 Results 74

4.4 Discussion and Conclusion 82

References **84**

References 84

5 Comparison of Different Models for Analysis of Renal Diffusion Imaging **91**

5.1 Introduction 93

5.2 Materials and Methods 95

5.2.1 Study population 95

5.2.2 Image Acquisition 95

5.2.3 Data Analysis 96

5.2.4 ROI positioning 97

5.2.5 Statistical analysis 97

5.3 Results 99

5.4 Discussion and Conclusion 107

References **109**

References 109

6 Summary and Outlook **115**

6.1 Summary 117

6.2 Outlook 118

References **119**

References 119

Chapter 1

Outline

This thesis describes the assessment of tissue microstructure using diffusion weighted magnetic resonance imaging. Chapters Two and Three describe the theory behind the experimental work presented in Chapters Four, Five, and Six.

Chapter Two introduces the principles of nuclear magnetic resonance (NMR) and magnetic resonance imaging (MRI) by starting with the Bloch Equation and different solutions under different circumstances. These provide the requisite background of MRI.

In Chapter Three, we review the basic grounding of DWI to support the material that is discussed the the later chapters. The imaging sequences and different models used in the subsequent experimental chapters are also introduced.

The following chapters report on the original contributions of this work.

In Chapter Four, the effect of the assessment of structural and mechanical properties of facial skeletal muscle with diffusion MRI is described.

Chapter Five describes the applicability of different diffusion models in renal pathology. Four models are studied as a function of the considered b-values and compared.

Chapter Six is the final chapter summarizing the experimental work presented in this thesis, and looking to some aspects for future study as well.

Chapter 2

Basic Principles of Magnetic Resonance Imaging

2.1 Introduction

Magnetic resonance imaging (MRI) is a medical imaging modality that uses magnetic fields to image the body noninvasively and without ionizing radiation. The fundamental physical principles of nuclear magnetic resonance (NMR) were discovered independently by Felix Bloch [1] and Edward Purcel [2] in 1946. They were both awarded the Nobel prize for Physics for this discovery. First MR images were obtained by Paul Lauterbur in 1973 [3] , who earned the Nobel price in Medicine in 2003 together with Peter Mansfield for their discoveries concerning MRI. In 1975, Richard Ernst [4] introduced an improved method of image acquisition, and was awarded the Nobel price in Chemistry in 1991. Certain atoms process a characteristic called nuclear spin angular momentum. Hydrogen atom, located throughout the human body mainly in the form of water, has a single proton and is the atom used in conventional MRI, which is called a spin. The spins create a small magnetic moment in the same direction as the angular momentum. Manipulating these spins through interactions with magnetic fields can generate the signal measured in MRI.

2.2 Magnetization

MRI is the imaging of magnetic moments that results from the quantum mechanical property of nuclear spin. The average behavior of many spins results in a net magnetization of the tissue $\overrightarrow{M}$.

In the absence of an external magnetic field, a set of nuclei has no bulk magnetization because the spin magnetic moments have independent and randomly distributed directions. In presence of a static magnetic field $\overrightarrow{B_0}$, the net magnetization tends to align in the direction of the field.

2.3 Three Magnetic Fields

MRI involves the interaction of these spins with three types of magnetic fields, which can be designed and controlled.

Main field: $\overrightarrow{B_0}$. Normally, the spins are in random directions, creating a 0 net magnetic moment. However, when a magnetic field is presented, magnetic moments can only align parallel or anti-parallel to the field. This main field is generated by superconducting coils or large permanent magnets. By convention, the direction of this static magnetic field is along the z-axis, the scanner axis, or the longitudinal direction.

$$\overrightarrow{B_0} = \begin{bmatrix} 0 \\ 0 \\ B_{z0} \end{bmatrix} = B_{z0}\overrightarrow{k} \tag{2.1}$$

where $\overrightarrow{k} = \begin{bmatrix} 0 \\ 0 \\ 1 \end{bmatrix}$ denotes the unit vector along z-axis.

Radio frequency field: $\overrightarrow{B_1}(t)$. The second magnetic field applied is a radio frequency (RF) field, called B_1 field. This field is usually perpendicular to $\overrightarrow{B_0}$, as an amplitude modulated sinusoid:

$$\overrightarrow{B_1}(t) = B_1 a_1(t) \begin{bmatrix} cos(\omega_0 t + \phi_1) \\ -sin(\omega_0 t + \phi_1) \\ 0 \end{bmatrix} \tag{2.2}$$

Field gradients: $\overrightarrow{G}$. To create an image, there needs to be spatially dependent information. Linear field gradients are applied to the main field. Paul Lauterbur and Peter Mansfield earned the 2003 Nobel Prize in Physiology or Medicine by developing, analyzing, and refining the use of gradient fields [3]. The magnitude of the field gradients varies at spatial coordinates. A general gradient can be expressed as

$$\begin{cases} \overrightarrow{G_x} = G_x \cdot x \cdot \overrightarrow{x} \\ \overrightarrow{G_y} = G_y \cdot y \cdot \overrightarrow{y} \\ \overrightarrow{G_z} = G_z \cdot z \cdot \overrightarrow{z} \end{cases} \tag{2.3}$$

where $\overrightarrow{x}$, $\overrightarrow{y}$, and $\overrightarrow{z}$ are unit vectors.

2.4 Bloch equations

In 1946, Felix Bloch derived a set of differential equations which describe the changes in the magnetization during precession, excitation and relaxation [1, 5].

2.4.1 Precession

When the spin magnetization vector $\overrightarrow{M}$ is placed in a magnetic field $\overrightarrow{B}$, $\overrightarrow{M}$ will experience a torque. The equation of motion for $\overrightarrow{M}$ is then:

$$\frac{d\overrightarrow{M}}{dt} = \gamma\overrightarrow{M} \times \overrightarrow{B} \tag{2.4}$$

which causes that the magnetization $\overrightarrow{M}$ will precess around a $\overrightarrow{B}$ field at

$$\omega = \gamma B \tag{2.5}$$

where ω is the Larmor frequency in megahertz (MHz), B is the strength of the magnetic field in Tesla (T), γ is the gyro-magnetic ratio, characteristic of the particle or the nucleus, for Hydrogen, $\gamma = 42.58 MHz/T$. The Larmor frequency of ^1H atoms in 1.5 T magnetic field is approximately 63 MHz.

2.4.2 Excitation

When a magnetic field is present, energy can be introduced into a stable spin system by applying an RF field perpendicular to the main field. This process is known as excitation of the spin system and can result in the longitudinal magnetization be tipped away from the z-axis toward the transverse plane. If the RF pulse is strong enough and applied long enough to tip the magnetization by exactly 90° (90° RF pulse), all of the longitudinal magnetization is flipped over and rotated into the transverse plane, Figure 2.1.

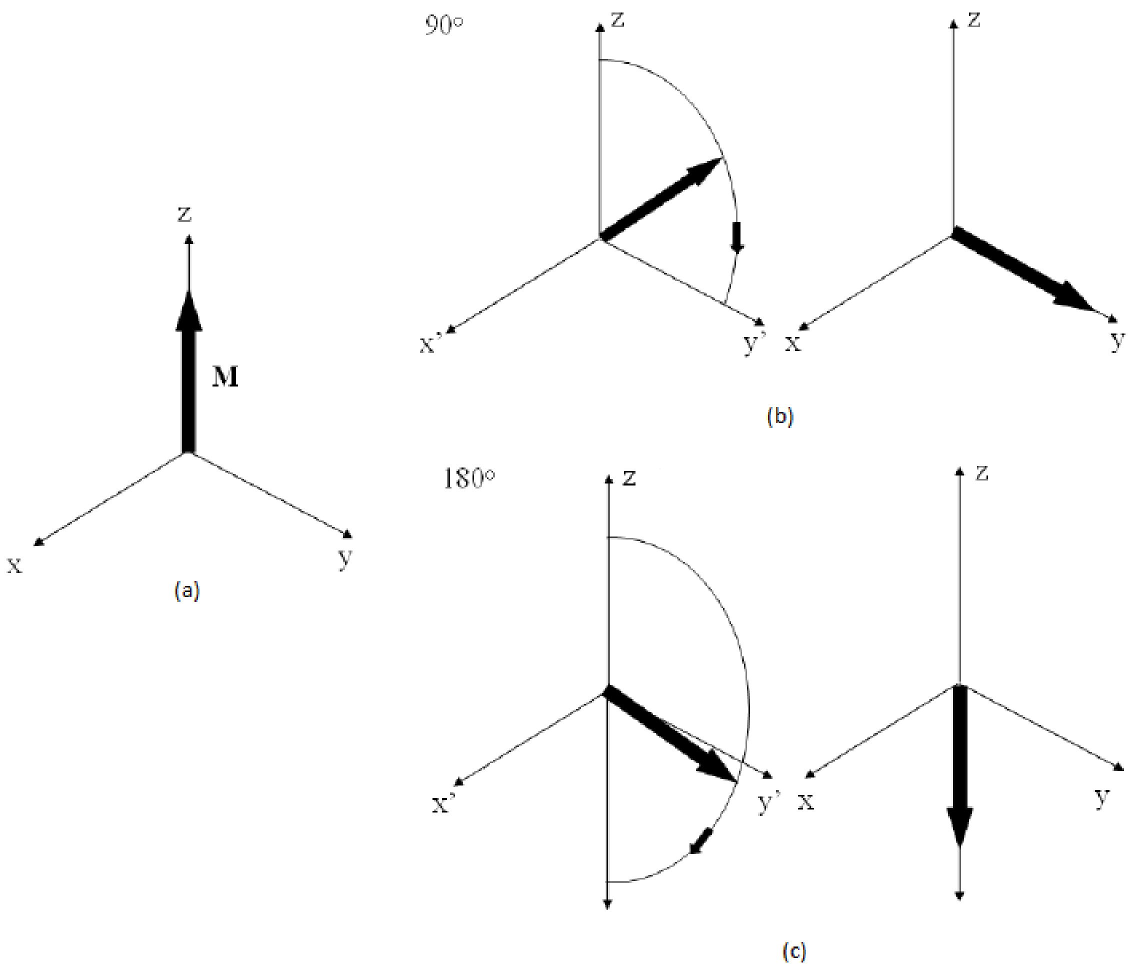

Figure 2.1: Magnetization in thermal equilibrium (a), and the process of a 90° (b) and 180° pulse (c).

The magnetic moments and hence the bulk magnetization precess about the overall magnetic field $\overrightarrow{B}(t) = [B_0 + \Delta B(t)]\,\overrightarrow{k}$, which is time-varying. Then the frequency of precession will turn to:

$$\omega(t) = \gamma\,[B_0 + \Delta B(t)] \tag{2.6}$$

To simplify the analysis, a rotating frame of reference is considered. The coordinate system for observation of the magnetization is rotating at a frequency, $\omega_0 = \gamma B_0$. In particular, the coordinate system is rotating about the z-axis in the same direction that $\overrightarrow{M}$ rotates about $\overrightarrow{B}$. In the laboratory frame of reference, the frame of reference is with coordinates (x, y, z). In this rotating frame, it has coordinates (x', y', z), and the magnetic fields $\overrightarrow{B_0}$ and $\overrightarrow{B_1}$ appear static.

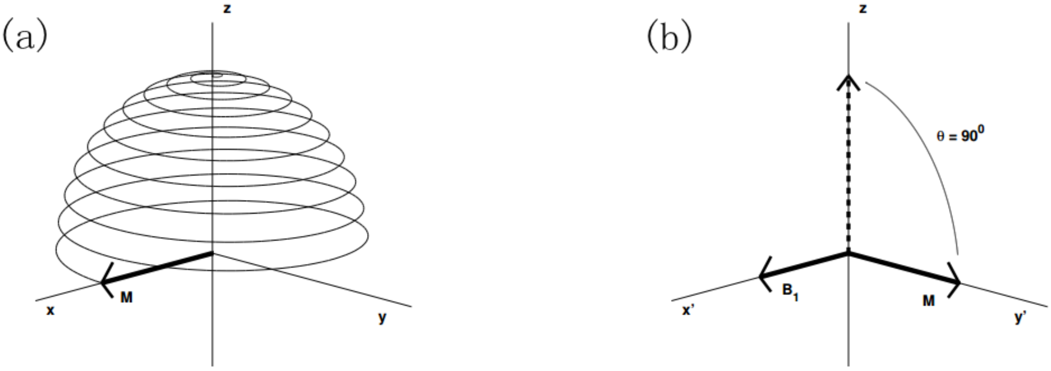

Figure 2.2: (a) Laboratory frame of reference, (b) Rotating frame of reference shares the longitudinal axis with the laboratory reference frame and rotate at the frequency of the excitation pulse.

For a rotation frame at ω_0, the coordinate axes are:

$$\begin{aligned} \overrightarrow{i'} &= \overrightarrow{i}\, cos(\omega_0 t) - \overrightarrow{j}\, sin(\omega_0 t) \\ \overrightarrow{j'} &= \overrightarrow{i}\, sin(\omega_0 t) + \overrightarrow{j}\, cos(\omega_0 t) \\ \overrightarrow{k'} &= \overrightarrow{k} \end{aligned} \tag{2.7}$$

If $\overrightarrow{M} = [m_x, m_y, m_z]$ and $\overrightarrow{M_{rot}} = [m_{x,rot}, m_{y,rot}, m_{z,rot}]$, then

$$\begin{gathered} m_{xy,rot} = m_{x,rot} + i m_{y,rot} = m_{xy} exp(i\omega_0 t) \\ m_{z,rot} = m_z \end{gathered} \tag{2.8}$$

When consider $\overrightarrow{B}(t) = [B_0 + \Delta B(t)]\, \overrightarrow{k}$. The magnetization in the rotation frame will appear to be precessing at

$$\omega_{rot}(t) = \gamma \left[B_0 + \Delta B(t)\right] - \omega_0 = \gamma \Delta B(t) \tag{2.9}$$

Thus, the effective $\overrightarrow{B}$ in the rotating frame is:

$$\overrightarrow{B_{eff}} = \overrightarrow{B} - \frac{\omega_0}{\gamma}\overrightarrow{k} = (B_0 + \Delta B(t) - B_0)\overrightarrow{k} = \Delta B(t)\overrightarrow{k} \tag{2.10}$$

Then, the Bloch equation can be written in the rotating frame as follow:

$$\frac{d\overrightarrow{M_{rot}}}{dt} = \overrightarrow{M_{rot}} \times \gamma\overrightarrow{B_{eff}} \tag{2.11}$$

When an RF pulse is applied, it is called forced precession because $\overrightarrow{M}$ is influenced by $\overrightarrow{B_1}$. After the RF pulse ends, the evolving magnetization is called free precession, because $\overrightarrow{M}$ processes around $\overrightarrow{B_0}$.

2.4.3 Relaxation

After switching off the RF pulse, particles begin to return to their thermal equilibrium state, aligned with the external field. This procession is associated with a loss of stored excess energy to surrounding particles which can be detected by the coil of the MRI scanner. Then we can observe two different types of relaxation processes. These two processes cause T1 relaxation and T2 relaxation, respectively.

2.4.3.1 T_1: Longitudinal Relaxation or spins-lattice relaxation

In T_1 relaxation, the nuclei can return to the thermal equilibrium only by dissipating their excess energy to their surroundings. This recovery process can be modeled by an exponential function characterized by a time constant T_1, the period for the longitudinal magnetization to recover 63% of its equilibrium value.

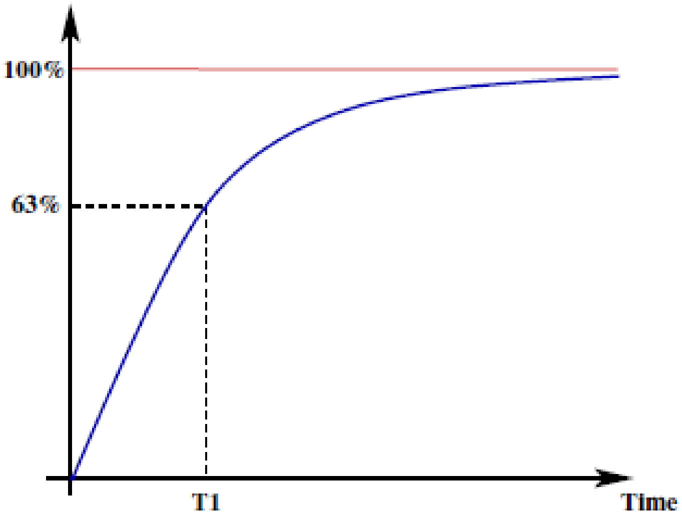

Figure 2.3: Longitudinal relaxation time T_1. Application of a 90° RF pulse causes longitudinal magnetization to be 0. After switching off this RF pulse, the longitudinal magnetization recovers back to the equilibrium. T_1 is the time that it takes the longitudinal magnetization to recover back to 60% of its final value.

When recovery from any reduction in $m_z$by RF excitation, it is governed by this equation:

$$\frac{dM_z}{dt} = -\frac{(M_z - M_0)}{T_1} \tag{2.12}$$

where M_0 is the equilibrium magnetization.

The general solution to this equation is:

$$M_z(t) = M_0 + (M_z(0) - M_0)exp\left(-\frac{t}{T_1}\right) \tag{2.13}$$

Then we can get:

1. After a 90 degree RF pules:

$$\begin{gathered} M_z(0) = 0 \\ M_z(t) = M_0\left(1 - exp\left(-\tfrac{t}{T_1}\right)\right) \end{gathered} \tag{2.14}$$

2. After a 180° inversion pulse,

$$\begin{aligned} M_z(0) &= -M_0 \\ M_z(t) &= M_0\left(1-2exp\left(-\tfrac{t}{T_1}\right)\right) \end{aligned} \tag{2.15}$$

3. After an α pulse:

$$\begin{aligned} M_z(0) &= M_0 cos\alpha \\ M_z(t) &= M_0\left(1-(1-cos\alpha)exp\left(-\tfrac{t}{T_1}\right)\right) \end{aligned} \tag{2.16}$$

T_1 is dependent on the strength of the external magnetic field and the internal motion of the molecules.

2.4.3.2 T_2 / T_2^*: Transverse Relaxation or spin-spin relaxation

T_2 relaxation refers to the loss of net magnetization in the transverse plane related to the dephasing of the spins following their phase coherence without energy dissipation after the RF pulse is switched off. The dephasing is an exponential decay process characterized by a time constant T_2, which corresponds to the period for the transverse component to loose 63% of its value just after the RF pulse.

This is governed by the equation:

$$\frac{dM_{xy,rot}}{dt} = -\frac{M_{xy,rot}}{T_2} \tag{2.17}$$

The general solution to the above equation is:

$$M_{xy,rot}(t) = M_{xy,rot}(0)exp\left(-\frac{t}{T_2}\right) \tag{2.18}$$

Then we can get:

1. After a 90 degree RF pules:

$$\begin{aligned} M_{xy,rot}(0) &= M_0 \\ M_{xy,rot}(t) &= M_0 exp\left(-\tfrac{t}{T_2}\right) \end{aligned} \tag{2.19}$$

2. After a 180° inversion pulse,

$$\begin{aligned} M_{xy,rot}(0) &= 0 \\ M_{xy,rot}(t) &= 0 \end{aligned} \tag{2.20}$$

3. After an α pulse:

$$\begin{aligned} M_{xy,rot}(0) &= M_0 sin\alpha \\ M_{xy,rot}(t) &= M_0\, sin\alpha\, exp\left(-\frac{t}{T_2}\right) \end{aligned} \tag{2.21}$$

T_2 is always less than or equal to T_1.

This dephasing described above actually is increased by intrinsic inhomogeneities, resulting in an overall signal decay that is even faster than that described by T_2. This type of decay is called T_2^*. The loss of the MR signal due to T_2^* effects is free induction decay (FID). T_2 relaxation denotes the process of energy transfer between spins, and T_2^* reflects the effects of additional field inhomogeneities contributing to dephasing. The relationship between T_2 from molecular processes and that from inhomogeneities in the magnetic field (T_2') is as follows:

$$\frac{1}{T_2^*} = \frac{1}{T_2} + \frac{1}{T_2'} \tag{2.22}$$

Dephasing induced by local field inhomogeneities can be reverted by applying a refocusing RF pulse (in an experiment called spin echo), thus recovering the magnetization due to pure T_2 decay [6].

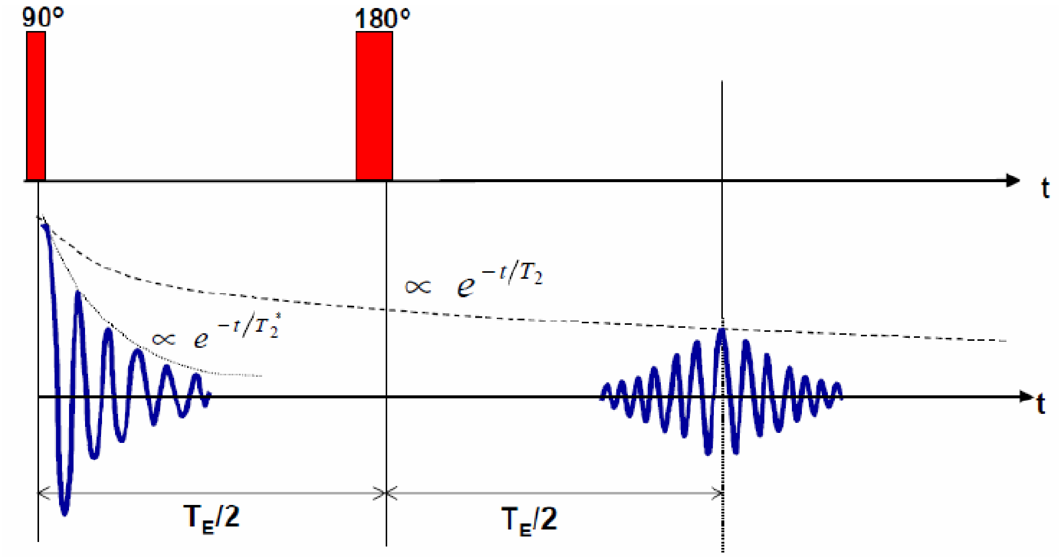

Figure 2.4: Formation of spin echo sequence. Application of a 90° RF pulse results in an immediate FID, which rapidly dephases due to T_2^* effects. After TE/2 time, a 180° RF pulse is applied, the spins begins to rephase, forming a maximum signal, and then dephase again.

2.4.4 Full Bloch equation with relaxation

The full Bloch equation with relaxation then can be written as:

$$\frac{d\overrightarrow{M}}{dt} = \gamma\overrightarrow{M} \times \overrightarrow{B} - \frac{M_x\overrightarrow{i} + M_y\overrightarrow{j}}{T_2} - \frac{(M_z - M_0)\overrightarrow{k}}{T_1} \tag{2.23}$$

where $\overrightarrow{i}$, $\overrightarrow{j}$, and $\overrightarrow{k}$ are unit vector in x, y and z directions respectively.

This equation describes three phenomenons: precession, transverse decay, and longitudinal recovery.

2.5 Spatial encoding and k-space

2.5.1 Magnetic field gradients for imaging

The magnetization $\overrightarrow{M}$ can be imaged by manipulating the applied magnetic field, which was first introduced by Lauterbur in 1973 [3].

2.5.1.1 Slice selection

A pulse sequence is a series of RF pulses and / or magnetic field gradients applied to a sample to produce a specific form of MR signal. It is indeed possible to encode and thus recover the MR signal from specific slice in the volume of interest by means of RF and linear gradients applied along the 3 spatial directions. This is known as slice selection. A linear gradient is applied along one axis (for example, z-axis), thus modifying the Larmor frequency of the spins along that axis, and an RF pulse of the same frequency and bandwidth as the slice of interest is applied so that only those spins are excited .

With a slice selection gradient enabled, the Larmor frequency varies with slice position z:

$$\omega_0(\overrightarrow{r}) = \omega_0(x,\, y,\, z) = \gamma(B_0 + zG_z) \tag{2.24}$$

To excite the spins in a slice with the thickness of $\Delta z = W/(\gamma G_z)$, an RF pulse with bandwidth W at $\omega_1(\overrightarrow{r}) = \gamma(B_0 + G_z(z - z_0)$ should be applied, as shown in Figure 2.4:

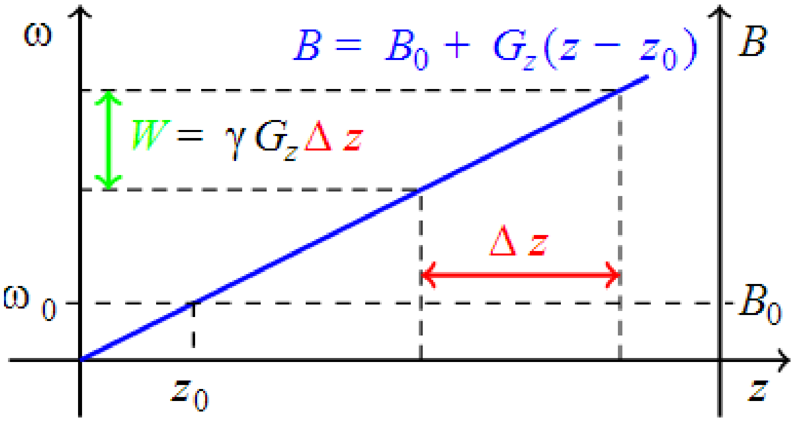

Figure 2.5: Slice selection: The frequency is varied through the application of a magnetic field gradient. Therefore, only spins in a slice with a thickness of Δz are excited because only these spins are in the right frequency bandwidth of the applied RF pulse.

The slice select gradient pulse is a positive portion followed by a negative portion with half of the duration, as shown in Figure 2.6. This is necessary to re-phase the MR signal , which is dephased by the slice select gradient, in order to get the maximum possible signal.

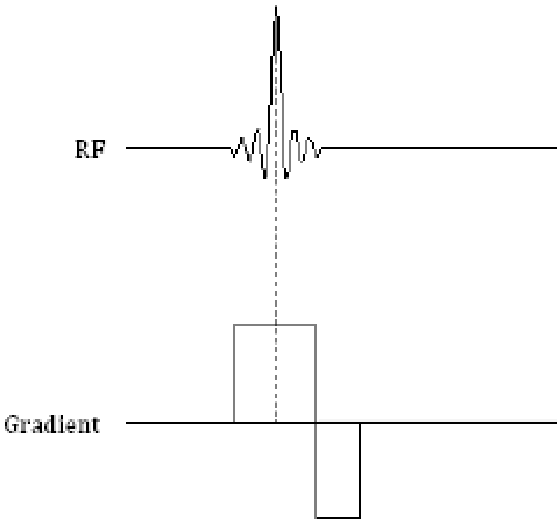

Figure 2.6: Slice selective RF pulse and gradient. The slice select gradient pulse is a positive portion followed by a negative portion with half of the duration.

The RF pulse typically used for slice selection is a sinc function in the time domain, and a square function in the frequency domain.

$$\overrightarrow{B}(\overrightarrow{r}) = \overrightarrow{B}(x,\, y,\, z) = \begin{bmatrix} 0 \\ 0 \\ B_0 + zG_z \end{bmatrix} = (B_0 + zG_z)\overrightarrow{k} \tag{2.25}$$

2.5.1.2 Frequency Encoding

After selecting slice position and thickness by application of an appropriate slice select gradient, spatial specificity needs to be incorporated into the measured signals. This is accomplished by spatial encoding, which comprises two steps, frequency encoding and phase encoding.

Frequency encoding uses a frequency encoding gradient, which is applied after the RF excitation, so this gradient only affects the spins in the excited slice. Commonly, it is applied along the x-axis (G_x):

$$\omega(x) = \gamma(B_0 + G_x x) \tag{2.26}$$

This FE gradient generates a magnetic field that increases linearly in strength along the x-axis, hence the corresponding changes in Larmor frequencies make spins on one side precess slower than the ones on the other side. When the MR signal is collected while the frequency encoding gradient is switched on, a whole frequency spectrum is obtained, in which high frequencies from one side and low frequencies from the other side.

2.5.1.3 Phase Encoding

Frequency encoding can only be done in one direction (x-axis). For the other direction (y-axis), the phase encoding of the signal takes place between the excitation and the readout.

$$\omega(y) = \gamma(B_0 + G_y y) \tag{2.27}$$

this can be rewritten in the rotating frame as:

$$\omega(y) = \gamma G_y y \tag{2.28}$$

If the phase encoding gradient is on for a time t_p , then this gradient introduces a phase difference:

$$\varphi(t) = \omega(y)t_p = \gamma G_y y t_p \tag{2.29}$$

After this gradient is switched off, this results in all the spins precessing in the same frequency but in different phases. This phase difference lasts until the signal is recorded. The accumulated phase is proportional to the gradient strength and to the location.

2.5.2 An example: Gradient Echo Imaging

Figure 2.7 (a) shows a basic imaging technique : gradient echo sequence [7]. In this sequence, after exciting only those spins which lie in one slice plane, a phase encoding gradient is applied along the y-axis and cause the spins to precess at a frequency determined by their y position to give information of the y-position. Next a frequency encoding gradient is applied along the x-axis and the FID is collected, and give information of the x-position.

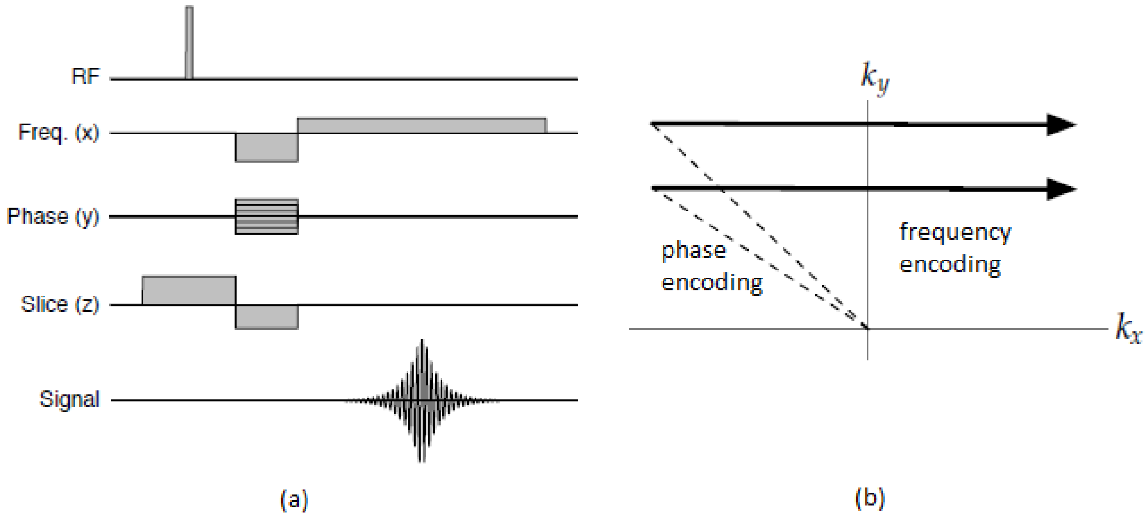

Figure 2.7: Pulse sequence (a) and k-space trajectory (b) for gradient echo imaging

2.5.3 K-space

If a phase encoding gradient of strength G_y is applied for a time t_p during the phase encoding, and then a frequency encoding gradient G_x is applied, $\rho(x, y)$ is the proton density, the signal and phase recorded at time t is given by:

$$\begin{gathered} S(t) = \iint_{x,y} \rho(x, y)e^{\varphi(t)}dxdy \\ \varphi(t) = \omega_0 t + \gamma G_x x t + \gamma G_y y t_p \end{gathered} \tag{2.30}$$

which can be written as:

$$S(t) = \iint_{x,y} \rho(x, y)e^{i\gamma G_x xt + i\gamma G_y y t_p}dxdy \tag{2.31}$$

let $k_x = \gamma G_x t$ and $k_y = \gamma G_y t_p$, the above function can be rewritten as:

$$S(k_x, k_y) = \iint_{x,y} \rho(x, y)e^{-ik_x x - ik_y y}dxdy \tag{2.32}$$

which is the 2D Fourier transform of the proton density and T_1/T_2decays (depending on the sequence). Therefore, $\rho(x,y)$ is an inverse FT of the detected signal:

$$\rho(x,y) = FT^{-1}[S(k_x,k_y)] = \iint_{k-space} S(k_x,k_y)e^{ik_xx+ik_yy}dk_xdk_y \tag{2.33}$$

So the single step is equivalent to sampling one line in the k_x direction of k-space. To cover the whole of k-space, it is necessary to repeat the sequence scheme as many times as the phase encoding steps required.

$$k_x = \gamma\int_0^t G_x(\tau)d\tau \tag{2.34}$$

The timing diagram in figure 2.7 (b) shows that, after the RF pulse is applied, to step through k-space, k_y phase encoding gradients are applied along the y-axis to collect the position information in the phase of the signal. Immediately afterward, k_x frequency encoding gradient is applied, and is maintained while the signal is sampled. A negative gradient is initially applied to move in the negative k_x, then a positive gradient of twice the duration is then applied to cover the whole of k_x. This combination of frequency and phase encoding allows to spatially locate the signal in a two-dimensional plane.

2.6 Image contrast

Different biological tissues have different concentration of hydrogen, which leads to different T1 and T2 relaxation times in different tissues. Therefore, we can get different image contrasts by manipulating the sequences.

As described in 2.4.3.1, the z component of the magnetization recovers after a 90 degree excitation is:

$$M_z(t) = M_0 \left(1 - exp\left(-\frac{t}{T_1}\right)\right) \tag{2.35}$$

If TR is not long compared to T_1, then all of the magnetization will not be able to recover to the initial magnetization M_0, but will be $M_0 \left[1 - exp(-\frac{TR}{T_1})\right]$.

A short TR results in T_1- weighted images. In T_1- weighted images, tissues with short T_1 appear bright, and the tissues with long T_1 are dark, because very little magnetization can be recovered for the next excitation pulse.

In Spin-Echo sequence, the observed magnetization will be:

$$M_{xy,rot}(TE) = M_0 exp\left(-\frac{TE}{T_2}\right) \tag{2.36}$$

In Gradient Echo sequence, if we use a α excitation pulse, the observed magnetization will be:

$$M_{xy,rot}(t) = M_0 \frac{sin\alpha \times exp\left(-\frac{TE}{T_2^*}\right)}{1 - cos\alpha \times exp(-\frac{TR}{T_1})} \tag{2.37}$$

From Equation 2.35 and Equation 2.36, the contrasts of the two sequences are the same if the excitation pulse is 90 degree. In that case, the only difference is that the

Spin Echo sequence gets rid of the dephasing inherent to field inhomogeneities, hence a T_2 dependency, while the Gradient Echo sequences depend upon the shorter T_2^*time.

A long TE results in T_2 - weighted images. In T_2 - weighted images, tissues with long T_2 appear bright, and the tissues with short T_2 appear dark, because their signal has completely decayed.

For both sequences, the impact of T_1 on the contrast is weighted by TR, and the impact of T_2 is weighted by TE. A long TR and short TE sequence is usually called Proton Density - weighted. A short TR and short TE sequence is usually called T1-weighted. And a long TR and long TE sequence is usually called T2-weighted

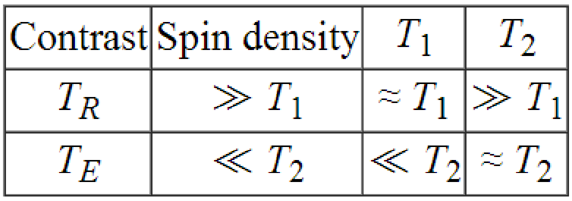

Contrast	Spin density	T_1	T_2
T_R	$\gg T_1$	$\approx T_1$	$\gg T_1$
T_E	$\ll T_2$	$\ll T_2$	$\approx T_2$

Figure 2.8: Basic MR contrasts and corresponding choices of TE and TR for Spin Echo sequences

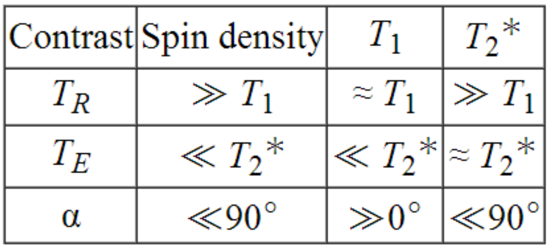

Contrast	Spin density	T_1	$T_2{}^*$
T_R	$\gg T_1$	$\approx T_1$	$\gg T_1$
T_E	$\ll T_2{}^*$	$\ll T_2{}^*$	$\approx T_2{}^*$
α	$\ll 90°$	$\gg 0°$	$\ll 90°$

Figure 2.9: Basic MR contrasts and corresponding choices of TE, TR and flip angle α for Gradient Echo sequences.

References

[1] F. Bloch, W. W. Hansen, and M. Packard, "Nuclear induction," *Physical Review*, vol. 69, pp. 127–127, Feb. 1946. 04331.

[2] E. M. Purcell, H. C. Torrey, and R. V. Pound, "Resonance absorption by nuclear magnetic moments in a solid," *Physical Review*, vol. 69, pp. 37–38, Jan. 1946. Cited by 2127.

[3] P. C. Lauterbur, "Image formation by induced local interactions: Examples employing nuclear magnetic resonance," *Nature*, vol. 242, pp. 190–191, Mar. 1973. Cited by 2867.

[4] A. Kumar, D. Welti, and R. R. Ernst, "NMR fourier zeugmatography," *Journal of Magnetic Resonance (1969)*, vol. 18, pp. 69–83, Apr. 1975. Cited by 0766.

[5] F. Bloch, "The principle of nuclear induction," *Science*, vol. 118, pp. 425–430, Oct. 1953. 00035.

[6] E. Hahn, "Spin echoes," *Physical Review*, vol. 80, pp. 580–594, Nov. 1950. 04291.

[7] J. M. S. Hutchinson, W. A. Edelstein, and G. Johnson, "A whole-body NMR imaging machine," *Journal of Physics E: Scientific Instruments*, vol. 13, p. 947, Sept. 1980. 00144.

Chapter 3

Diffusion MRI theory

3.1 Physics of Diffusion

3.1.1 Free diffusion

The free diffusion is the random motion that originates when the molecules collide with other molecules. The motion was discovered in 1827 by Robert Brown, and called a Brownian motion. The distribution can be described by a Gaussian probability density function.

Free diffusion is caused by thermal mobility of the molecules. The Brownian motion of the molecules occurring due to their thermal energy motion. To explain this phenomenon, the Fick's first law was suggested which relates the diffusive flux to any concentration difference through the relationship

$$\mathbf{J} = -D \bigtriangledown C \tag{3.1}$$

where J is the net particle flux (vector), C is a local concentration of particles, and D is called the diffusion coefficient which is the temperature dependent $[m^2/s]$.

The change in concentration as a function of time can be written like

$$\frac{\partial \mathrm{C}}{\partial t} = D \bigtriangledown^2 C \tag{3.2}$$

which is Fick's second law, also known as the diffusion equation.

Using the displacement distribution concept, in 1905, Einstein [1] was able to derive an explicit relationship between the mean squared displacement of the ensemble and the diffusion coefficient, characterizing the Brownian motion by

$$< S^2 >= 2nD\Delta \tag{3.3}$$

where $< S^2 >$ is the mean squared displacement of particles, n is the dimension, Δ is the diffusion time, and D is the classical diffusion coefficient appeared in Fick's first and second laws above.

3.1.2 Restricted Diffusion

In Brownian motion, molecules diffuse freely in all directions. With a distribution width that expands with time, both the conditional probability and averaged propagator exhibit a Gaussian distribution over molecular displacements .

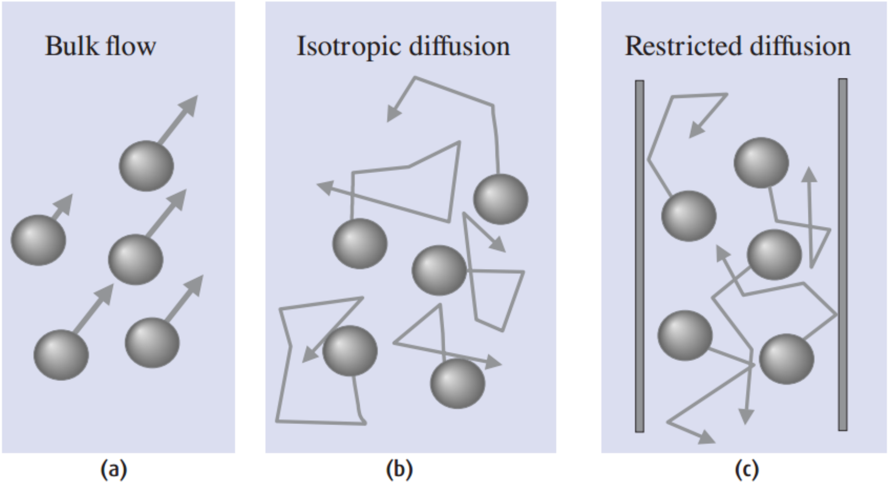

Figure 3.1: Three types of molecular motion (indicated by arrows) which may occur in tissue (a) bulk flow, (b) isotropic diffusion where molecular motion is random and (c) restricted diffusion where random motion is constrained by physical barriers, e.g. by cell membranes [2].

However, within the tissue, the random motion of water molecules is influenced by a variety of factors such as restrictions due to cell membranes, cytoskeleton, and macromolecules. By employing the understanding of how micro structural features contribute to the overall diffusional process, it may be possible to obtain valuable information about the biological micro structure simply by observing the motion of water molecules. This is particularly important in the understanding of tissue with complicated structure.

3.2 Diffusion weighting

3.2.1 Diffusion weighted imaging with Spin Echoes

Magnetic resonance provides a unique opportunity to quantify the diffusional characteristics of a wide range of specimens. Because diffusional processes are influenced by the geometrical structure of the environment, MR can be used to probe the structural environment non invasive. This is particularly important in studies that involve biological samples in which the characteristic length of the boundaries influencing diffusion are typically so small that they cannot be resolved by conventional MRI techniques.

The sensitivity of the spin-echo MR signal on molecular diffusion was recognized by Hahn. He reported a reduction of signal of the spin echo and explained it in terms of the dephasing of spins caused by translational diffusion within an inhomogeneous magnetic field [3]. While he proposed that one could measure the diffusion coefficient of a solution containing spin labeled molecules, he did not propose a direct method for doing so.

In 1965, Stejskal and Tanner [4] introduced a pulsed gradient spin echo (PGSE) sequence that made diffusion measurements by MRI possible, which is also well known as the Stejskal and Tanner sequence. Typically, it is applied using 90° and 180° RF pulses, and two gradients are applied as in the following Figure 3.1. In this technique, a clear distinction between the encoding time (pulse duration, δ) and the diffusion time (separation of the two pulses, Δ).

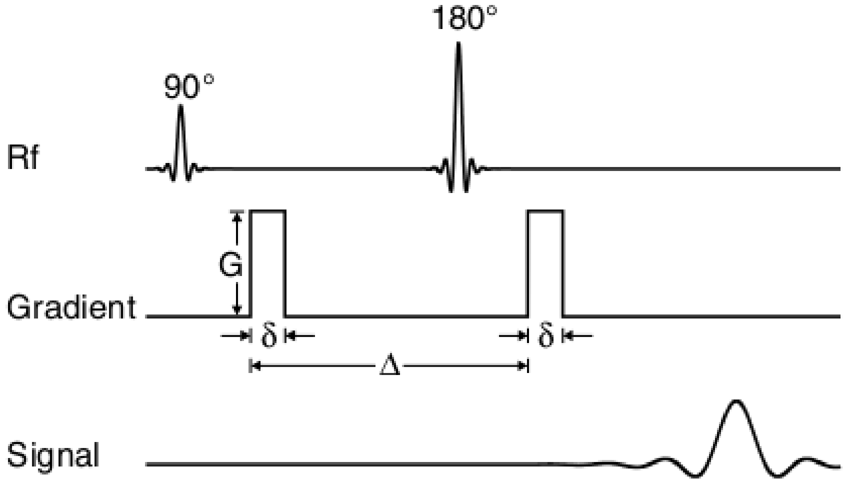

Figure 3.2: Schematic timing diagram of the PGSE sequence with diffusion gradients. δ is the gradient pulse duration, Δ is the time between the start of the two gradient pulses, G is the gradient strength.

and together with this pulse sequence, Le Bihan and Breton in 1985 [5] introduced this equation:

$$S(b) = S(0) \cdot e^{-b \cdot D} \tag{3.4}$$

where S(b) is the diffusion weighted signal and S(0) is the signal without diffusion weighting acquired for the same TE. The b-value is the diffusion sensitivity and describes the relationship between the diffusion coefficient D, and the signal attenuation. The b-value is defined by

$$b = \gamma^2 G^2 \delta^2 T_d \tag{3.5}$$

where G is the amplitude of diffusion encoding gradient and δ is the duration of the gradient pulse (see Figure 3.2), γ is the gyro-magnetic ratio and T_d is the effective diffusion time which is defined as

$$T_d = \Delta - \frac{\delta}{3} \tag{3.6}$$

3.2.2 Diffusion MR Imaging with Echo Planar Imaging Techniques (EPI)

When Stejskal-Tanner diffusion gradients are added to a conventional multiple pulse MR imaging sequence to sensitize the image to the effect of microscopic motion of water molecules, the image becomes very sensitive to bulk motions. To avoid this problem, an Echo Planar Imaging technique (EPI), with additional diffusion weighting gradient pulses, was used [6]. In this technique, after a single RF excitation, a train of echoes would be acquired with a short phase encoding gradient pulse between each echo.

3.2.2.1 Diffusion MR Imaging with single shot EPI

EPI is a fast MRI technique, making it possible to obtain many different diffusion weighted MR images in one session, enabling good accuracy diffusion maps to be calculated. The major advantages of EPI over conventional imaging are reduced imaging time with the potential for improved patient throughput, reduced motion artifact, and the ability to image rapid physiologic processes.

In single shot EPI, the entire k-space is acquired after a single RF excitation. An spin echo based diffusion weighted EPI sequence is shown in figure 3.3(a), and a diagram of k-space is displayed in figure 3.3 (b):

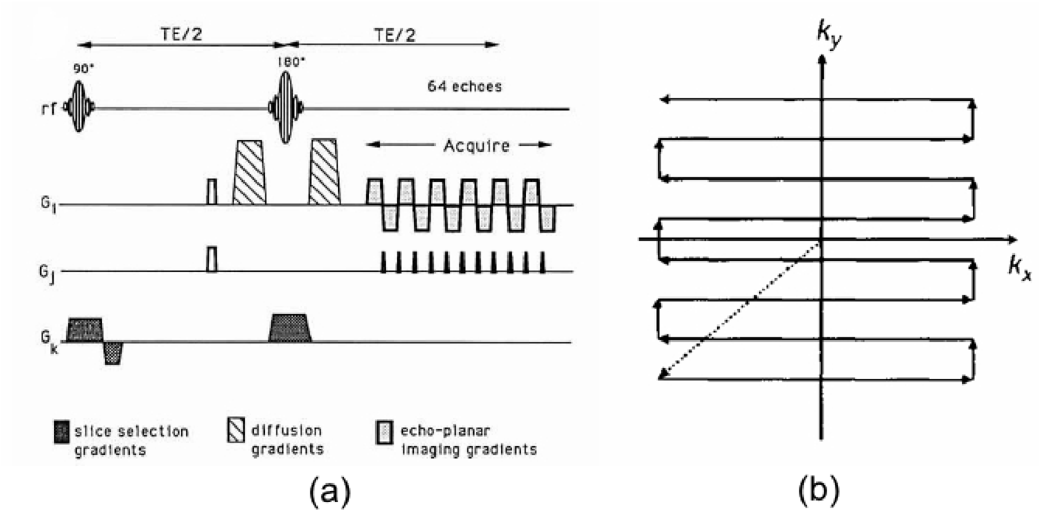
TE/2
TE/2
90°
180°
64 echoes
rf
Acquire
G_i
G_j
G_k
slice selection gradients
diffusion gradients
echo-planar imaging gradients
(a)
k_y
k_x
(b)

Figure 3.3: Diffusion weighted spin echo based single shot EPI sequence (a), and k-space trajectory (b) [6].

3.2.2.2 Diffusion MR Imaging with Multi-shot Interleaved EPI

However, diffusion weighted single-shot EPI has a number of limitations, including severe image distortions, suffering from a limitation to the maximum resolution that can be achieved, and long echo times. The major problems involved in single-shot EPI are the shortness in tissue of the transverse relaxation time T2 and the inhomogeneity related dephasing time T2*. If the time between the excitations and acquisition is too long, there would be no signal remains to be detected. So a multiple shot EPI was presented to avoid this problem.

In interleaved sequences, each repetition acquires every nth (n is the number of shots) line in k-space and for the complete raw data set the various repetition data are interlaced. A diagram of k-space is displayed in figure 3.4:

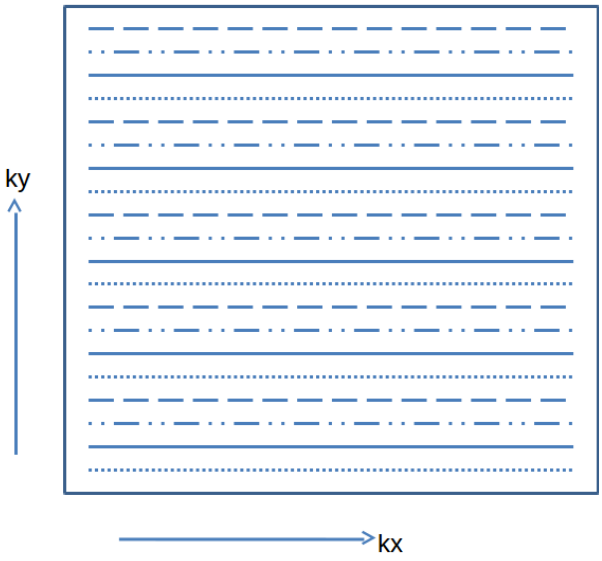

Figure 3.4: K-space trajectory of multi shot interleaved EPI

3.2.2.3 Diffusion MR Imaging with Multi-shot Readout-Segmented EPI

As shown in the following Figure 3.5 [7], after a diffusion preparation, two spin echoes were used to acquire imaging and navigator data, respectively, using a sinusoidal EPI readout, which sampled a subset of contiguous points in the readout direction. For the first spin echo, a variable amplitude prephasing gradient pulse (colored blue in Figure 3.5) was applied to define an offset along k_x, which was varied from one shot to the next. In this manner, each shot was used to sample a different segment in the k_x direction. The smaller readout gradient moment, corresponding to the reduced k_x coverage, allows a substantially shorter echo-spacing than with single-shot EPI, significantly reducing the effect of susceptibility and T_2^* decay. The second echo was used to generate 2D navigator data by sampling the central k_x segment at each shot. A blipped phase-encoding gradient was used to traverse the full k_y range.

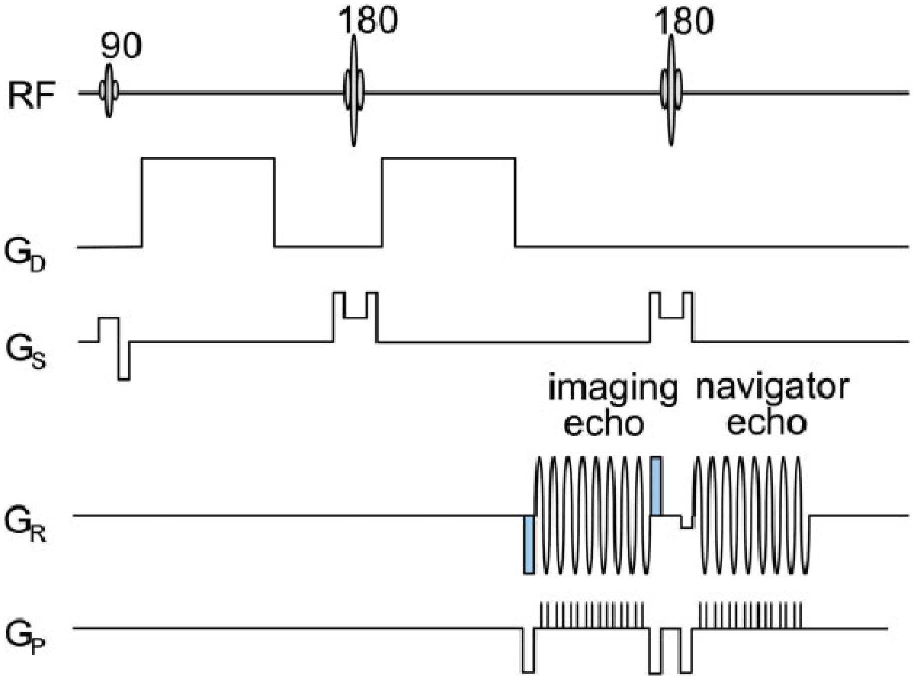

Figure 3.5: Sequence diagram for a single readout segment: Following a diffusion preparation (G_D), two spin echoes are used to sample imaging and navigator echo. For the first spin echo a variable amplitude prephasing gradient pulse (colored blue) is applied to define an offset along k_x, which varies from shot to shot to sample a different segment in k-space. For the second echo a constant amplitude prephasing gradient pulse is used to acquire the central k_x segment very time [7].

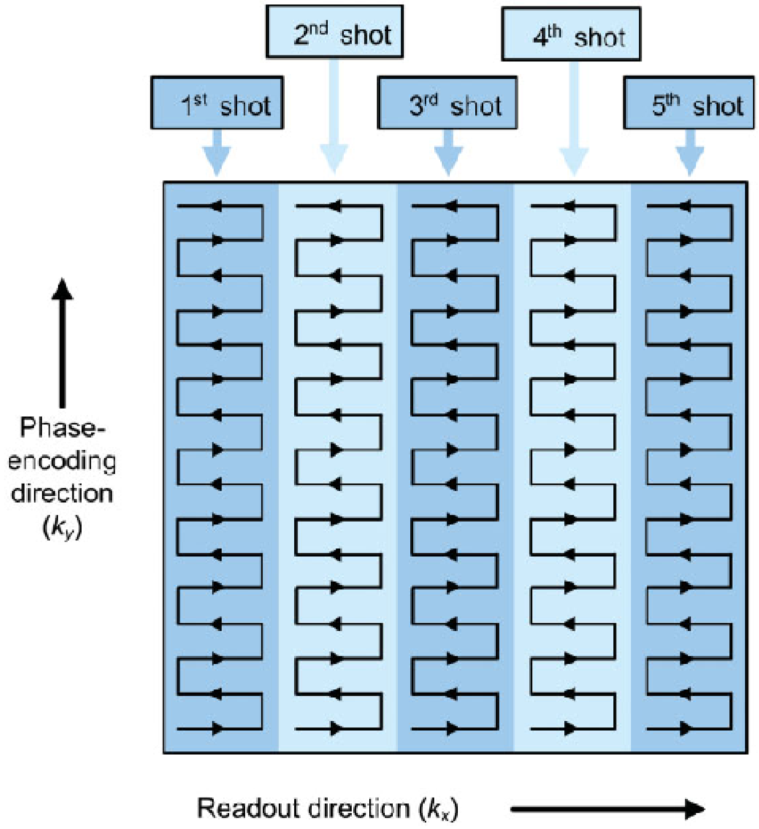
2nd shot
4th shot
1st shot
3rd shot
5th shot
Phase-encoding direction (k_y)
Readout direction (k_x)

Figure 3.6: Depiction of the k-space coverage for readout segmented EPI. In this example, a five-shot EPI acquisition is used, which divides k-space into five segments along the readout direction. Each shot acquires data from a set of contiguous k-space sample points, which is beneficial for 2D navigator phase correction. In practice, a small overlap is used at the interface between readout segments [7].

This multi-shot readout segmented EPI technique can be used to acquiring DW images, which have low susceptibility based image distortion and T2* blurring and a robust correction for motion-induced phase artifact.

3.2.3 Diffusion MR Imaging with Steady-State Free Precession (SSFP)

Diffusion weighted SE is widely used currently. When combined with a 2D, single shot EPI, it is a powerful method due to its relatively high efficiency, ability to obtain strong diffusion weighting and insensitivity to motion. However, this method has a number of limitations, including severe image distortions, limited resolution and long echo times. As a result, several other DWI techniques have been developed, including diffusion weighted Steady-State Free Precession (DW-SSFP) imaging technique

3.2.3.1 Steady-State Free Precession (SSFP)

Steady-state free precession (SSFP) is a kind of fast imaging technique, which has been used widely in numerous MRI applications. SSFP was first introduced by Carr in 1958 [8], and also presented by Freeman and Hill [9] and Hinshaw [10] in the 1970s.

When the same sequence of RF rotations, precession and relaxation is repeated, a steady-state forms, where the magnetization at some point in the sequence is the same from one TR to the next, There are three cases:

- $TR \gg T_1$ and $TR \gg T_2$. The magnetization at the start of the sequence relaxes completely to the equilibrium magnetization, M_0.
- $TR \gg T_2$ but $TR \ll T_1$. All transverse magnetization will be 0 at the start of the sequence, but the longitudinal magnetization cannot return to thermal equilibrium before each new excitation. The longitudinal magnetization can reach a steady-state after several TRs.
- $TR \ll T_1$ and $TR \ll T_2$. Both transverse magnetization and longitudinal magnetization can not relax back to thermal equilibrium. After a certain number of excitations, a dynamic steady-state builds up.

3.2.3.2 Steady-State diffusion weighted imaging

The diffusion sensitivity of SSFP pulse sequences was first presented by Kaiser, Bartholdi, and Ernst (KBE) in 1974 [11]. Then LeBihan [12] [13], Merboldt [14, 15], Patz [16], Wu [17], Buxton [18] reported DWI with SSFP.

DW-SSFP has long been recognized to offer potential benefits over conventional spin-echo methods. This family of pulse sequences is highly efficient and compatible with three-dimensional acquisitions, which could enable high-resolution, low-distortion images. However, the same properties that lead to its efficiency make steady-state imaging highly susceptible to motion and create a complicated signal with dependence on T1, T2 and flip angle [19].

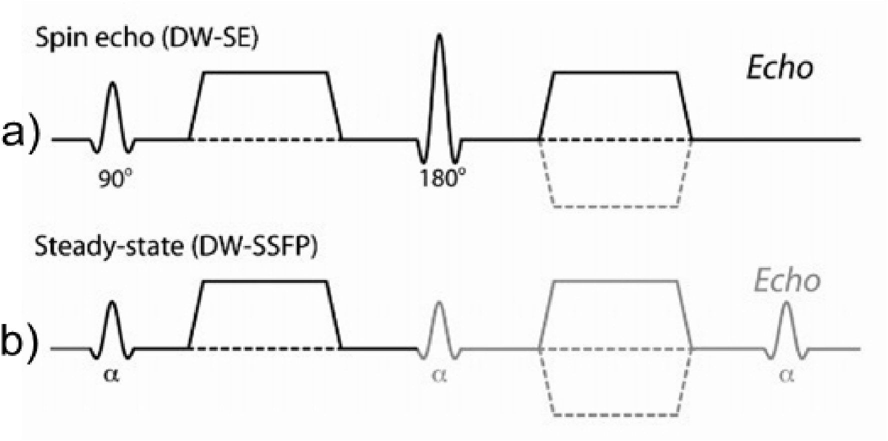

Figure 3.7: Diffusion-weighting schemes for (a) spin echo, and (b) SSFP. The implicit negation of gradients due to 180° inversion of the magnetization is indicated with gray, dashed lines. For SSFP, multiple repetition periods are shown to emphasize the similarity of diffusion contrast to SE. For illustration purposes, the timescales of the different sequences are matched, but in general this will not be the case [20].

3.2.3.3 Diffusion weighted Double Echo Steady-State Free Precession (DW-DESS)

As an extension of DW-SSFP, Diffusion weighted Double Echo Steady-State Free Precession (DW-DESS) technique is introduced by Bieri et.al. [21] using a double-echo steady-state approach, which is relaxation time independent. In this technique, two primary echo paths (FID and Echo) are separated by a large unipolar diffusion-sensitizing gradient dephasing moment (Gt). From the simultaneous acquisition of both, the FID and Echo signal, relaxation independent information about the molecular diffusion constant D can be extracted.

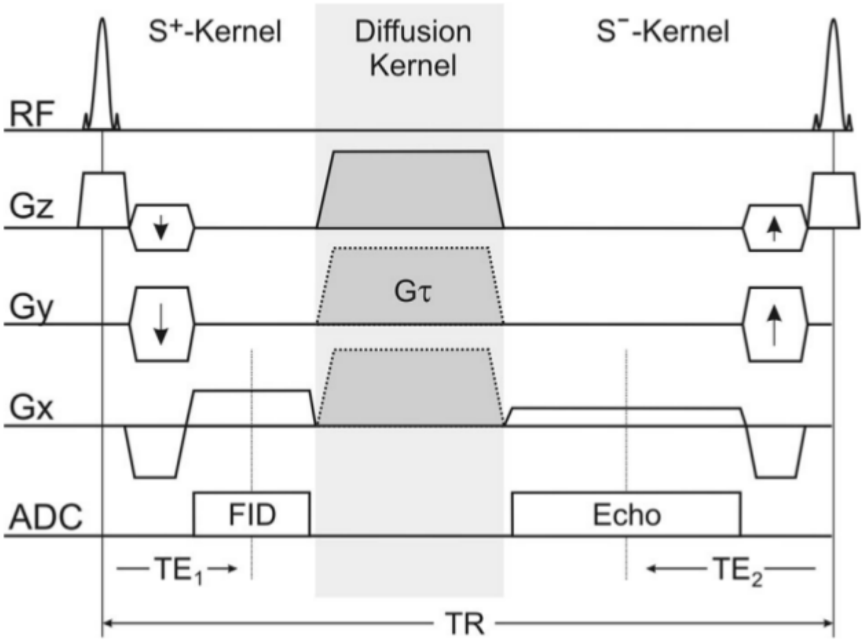
S⁺-Kernel
Diffusion Kernel
S⁻-Kernel
RF
Gz
Gy
Gτ
Gx
ADC
FID
Echo
TE1
TE2
TR

Figure 3.8: Diffusion-weighted double echo steady state (dwDESS). The two primary echo paths (FID and Echo) are separated by a large unipolar diffusion-sensitizing gradient dephasing moment (G_τ). From the simultaneous acquisition of both, the FID and Echo signal, relaxation independent information about the molecular diffusion constant D can be extracted [21].

3.3 Models

3.3.1 The Mono-exponential Model: Apparent diffusion coefficient ADC

The ADC is the diffusion coefficient that can be determined from the Stejskal-Tanner equation if at least two different b-values have been measured.

$$D = \frac{ln\left(\frac{S(b_1)}{S(b_2)}\right)}{b_1 - b_2} \tag{3.7}$$

The in vivo diffusion coefficient is denoted ADC since biological effect affects the value.

The signal attenuation is reduced to a simple, convenient, mono-exponential expression:

$$S(b) = S(0) \cdot e^{-b \cdot D} \tag{3.8}$$

where S(b) is the diffusion weighted signal and S(0) is the no diffusion weighted signal acquired for the same TE. The b-value is the diffusion sensitivity and describes the relationship between the diffusion coefficient D, and the signal attenuation.

3.3.2 The Bi-exponential Model: intravoxel incoherent motion (IVIM)

The ADC in tissue is smaller than free water diffusion in an aqueous solution. Furthermore, many studies have experimentally established that the water diffusion-sensitized MRI signal attenuation in tissue as a function of the b-values could not be well described by a single exponential decay, which would have been expected in the free Brownian diffusion [22–25]. High viscosity, macromolecular crowding and restriction effects have been proposed to explain the water diffusion reduction in the intracellular space, and tortuosity effects for water diffusion in the extracellular space. With restricted diffusion, the displacements of the molecules become limited when they reach the boundaries of close spaces and the ADC goes down with longer diffusion times. Furthermore, the overall low diffusivity of water in cells could not be well explained by true restriction effects resulted from cell membranes nor by scattering or obstruction effects from cellular macromolecules. This strongly suggests that the cellular components responsible for the reduced diffusion coefficient in biological tissues are much smaller than the diffusion length currently used with MRI.

Le Bihan et al [26], in pioneering work on intravoxel incoherent motion (IVIM) modeling of DWI, suggested that movement of blood in micro vasculature could be modeled as a pseudo diffusion process, which is measurable at low b values ($<200\text{s/mm}^2$). THE IVIM is also referred to as micro circulation or perfusion. Theses effects can be resolved from true tissue diffusion by using sufficient b-values sampling and a bi-exponential curve fit analysis, which resolves tissue diffusion and pseudo diffusion coefficients separately along with their respective volume fraction. Furthermore, these IVIM parameters may provide measurements that are independent of the b values used for imaging, as long as sufficient b values are sampled in both low and high b value regimen.

In this model:

$$S = S(0) \cdot \{f_{fast} \cdot exp(-b \cdot D_{fast}) + f_{slow} \cdot exp(-b \cdot D_{slow})\} \tag{3.9}$$

f and D are the volume fraction and the diffusion coefficient associated to the slow and fast diffusion phases, with $f_{slow} + f_{fast} = 1$. In this model, differences in T2 relaxation are not taken into account. IVIM MRI was initially introduced to evaluate perfusion and produce maps of brain perfusion, for brain activation studies and clinical applications [27–30] .

The problem with this bi-exponential model is that the nature of the two diffusion pools has remained exclusive. It has been often considered that the extracellular compartment might correspond to the fast diffusion, as water would be expected to diffuse more rapidly there than in the intracellular, more viscous compartment. However, the volume fractions of the two water phases obtained using the bi-exponential model do not agree with those known for the intracellular and extracellular water fractions. And also, some careful studies have shown that such bi-exponential diffusion behavior could also be seen solely within the intracellular compartment, pointing out that both the slow diffusion and fast diffusion phases probably coexist within the intracellular compartment.

This bi-exponential shape of the diffusion attenuation would also remain valid in the presence of two water pools when the exchange regime becomes intermediate, but one has to replace the values for $f_{slow,fast}$ and $D_{slow,fast}$ in the above equation by more complex parameters taking also into account the residence time of the molecules in the fast and slow components relative to the measurement time in a more realistic manner.

3.3.3 The Stretched-exponential Model

Two types of heterogeneity can be defined in MRI diffusion experiments: intravoxel and inter-voxel. However, as described in the last section, mono-exponential or bi-exponential signal models may have a physical basis in separate parenchymal proton pools, but one must also consider the possibility that a continuous distribution of diffusion coefficients arises from a multiplicity of pools. Based on these, Bennett et al [31,32] introduced another diffusion model, which is called stretched exponential model:

$$S(b) = S(0) \cdot exp\{-(b \times DDC)^{\alpha}\} \tag{3.10}$$

Where α is the stretching parameter, which characterizes the deviation of the signal attenuation from mono-exponential behavior, and is limited to values between zero and one. A value of α that is near one indicates high homogeneity in apparent diffusion, namely a highly mono-exponential attenuation curve. Lower values of α result from non-exponential behavior which is caused by the addition of multiple separable proton pools within the voxel.

This function has been applied to describe non-exponential diffusion in neural tissue. There are two free parameters in the model of the above equation: the distributed diffusion coefficient (DDC) and α . The DDC parameter refers to the diffusion coefficient quantity derived from fitting the stretched-exponential function to the data.

3.3.4 The Kurtosis Model

The diffusion of water through a biologic tissue can be regarded as a random process. Thus, the chance of a particular water molecule diffusing from one location to another in a given period of time is governed by a probability distribution. In the simplest models, this is a Gaussian distribution, which is proportional to the diffusion coefficient. However, for time intervals on the order of tens of milliseconds, the complex structure of most tissues, consisting of various types of cells and their membranes, can cause the diffusion displacement probability distribution to deviate substantially from a Gaussian distribution. This deviation from Gaussian behavior can be quantified using a convenient dimensionless metric called the excess kurtosis [33]. Since the deviation from Gaussian behavior is governed by the complexity of the tissue, within which the water is diffusing, this excess diffusional kurtosis can be regarded as a measure of a tissue's degree of structure.

The Kurtosis model is based on the same type of pulse sequences employed for conventional diffusion weighted imaging, but the required b values are somehow larger than those usually used to measure diffusion coefficients. In the brain, b-values of about $2000 \mathrm{s/mm}^2$ are sufficient [34, 35], which can now be obtained on clinical MRI systems. Thus, diffusion kurtosis imaging (DKI) provides a practical clinical technique for quantifying non-Gaussian water diffusion and thereby for probing the microscopic structure of biologic tissues.

Diffusion kurtosis imaging has been proposed as a minimal extension of DTI that enables the quantification of non-Gaussian diffusion through the estimation of the diffusion kurtosis, a quantitative measure of the non-Gaussian of the diffusion process. Quantitative rotationally invariant diffusion metrics can be extracted from the DKI analysis, such as the mean kurtosis (MK), radial kurtosis and axial kurtosis.

Kurtosis comes from the second order of Taylor extended Stejskal and Tanner equation:

$$ln\left[S(b)/S(0)\right] = -bD_{app} + \frac{1}{6}b^2D_{app}^2K_{app} \tag{3.11}$$

where K_{app} is the apparent kurtosis coefficient (AKC), D_{app} is known as apparent diffusion coefficient.

This DKI approach differs essentially in that the imaging data are fit to a quadratic function, which allows for estimates of both the apparent diffusion coefficient and the diffusional kurtosis.

3.4 Diffusion Tensor Imaging

3.4.1 Diffusion Anisotropy

As mentioned above in 3.1.1 self diffusion, free diffusion, also called isotropic diffusion, occurs in pure liquids, and describes the finding that the self-diffusivity is the same in all directions. So, a single self-diffusion coefficient is enough to describe the phenomenon. But, in more complex media, self diffusivity was not sufficient to describe diffusive transport any more. So the apparent diffusion coefficient (ADC) was addressed to meet this deficiency, which also depends on tissue micro dynamics, micro structures, and gradient pulse parameters as well.

In even more complicated case, diffusion anisotropy, the measured diffusivity is not the same in all directions. The ADC depends on the angle between the diffuse direction and applied magnetic field gradient. The largest observed diffusion coefficient is observed when the diffusion sensitive gradient is parallel to the diffuse direction, and the smallest ADC is observed when the diffusion sensible gradient is perpendicular to the diffuse direction.

3.4.2 Diffusion Tensor

To quantify the diffusion anisotropy, a more general description uses a 3D model, and the diffusion is approximated by an effective diffusion tensor.

$$\boldsymbol{D} = \begin{bmatrix} D_{xx} & D_{xy} & D_{xz} \\ D_{yx} & D_{yy} & D_{yz} \\ D_{zx} & D_{zy} & D_{zz} \end{bmatrix} \tag{3.12}$$

The first subscript (x, y, z) refers to the natural orientation of the cells or tissue, and the second refers to the gradient orientation. So, $D_{xy} = D_{yx}$, $D_{xz} = D_{zx}$, $D_{zy} = D_{yz}$, hence the diffusion tensor is a symmetric matrix, with six independent values. Therefore, we get:

$$\boldsymbol{D} = \begin{bmatrix} D_{xx} & D_{xy} & D_{xz} \\ D_{xy} & D_{yy} & D_{yz} \\ D_{xz} & D_{yz} & D_{zz} \end{bmatrix} \tag{3.13}$$

After measurement of the diffusion constants in six selected directions, the diffusion anisotropy geometry can be described with the formalism of the 3D tensors introduced above.

Eigenvalues and eigenvectors decomposition of the tensor can be calculated according to :

$$\boldsymbol{De} = \lambda \boldsymbol{e} \tag{3.14}$$

or

$$(D - \lambda \boldsymbol{I})\boldsymbol{e} = 0 \tag{3.15}$$

in which, $\boldsymbol{I}$ is the identity matrix, has a nontrivial solution. In this formalism, the diffusion anisotropy is described by an ellipsoid whose three main axes may differ in length in proportion to the ADC in the corresponding direction. Increasingly accurate geometric models of the averaged structures that hinder diffusion in a voxel may be generated when additional diffusion constants for other directions are measured.

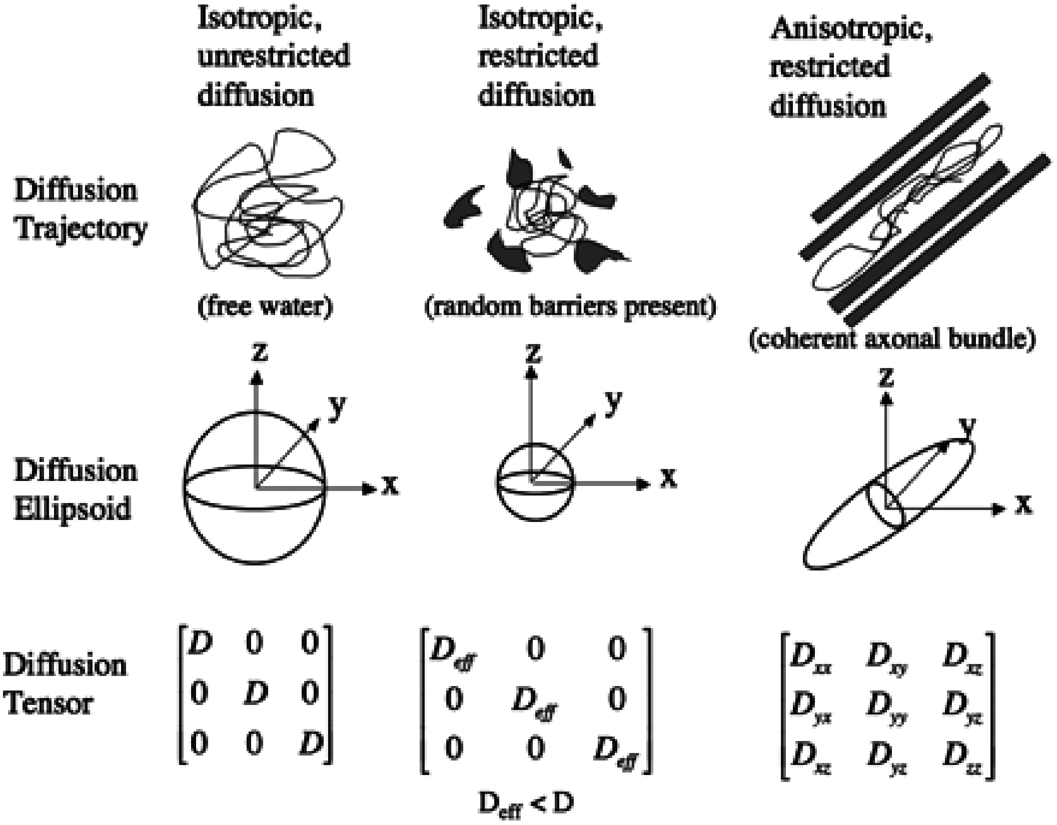
Isotropic, unrestricted diffusion
Isotropic, restricted diffusion
Anisotropic, restricted diffusion
Diffusion Trajectory
(free water)
(random barriers present)
(coherent axonal bundle)
Diffusion Ellipsoid
z
y
x
Diffusion Tensor
$\begin{bmatrix} D & 0 & 0 \\ 0 & D & 0 \\ 0 & 0 & D \end{bmatrix}$
$\begin{bmatrix} D_{eff} & 0 & 0 \\ 0 & D_{eff} & 0 \\ 0 & 0 & D_{eff} \end{bmatrix}$
$D_{eff} < D$
$\begin{bmatrix} D_{xx} & D_{xy} & D_{xz} \\ D_{yx} & D_{yy} & D_{yz} \\ D_{xz} & D_{yz} & D_{zz} \end{bmatrix}$

Figure 3.9: The diffusion ellipsoids and tensors for isotropic unrestricted diffusion, isotropic restricted diffusion, and anisotropic restricted diffusion [36].

3.4.3 Diffusion Tensor Imaging (DTI)

Diffusion Tensor Imaging (DTI) was introduced by Basser [37] [38], for the technique used to measure the full diffusion tensor. DTI is an extension of DWI, it measures diffusion in six or more directions, from which the diffusion tensor can be reconstructed. As the gradient coils in the MR system are fixed along the x, y, or z direction, a gradient in any direction can be created by using a combination of gradients in all directions.

3.4.4 DTI Fiber Tractography

DTI fiber tractography is an extension of diffusion tensor imaging, and can visualize the fibers in 3D. There are different algorithms to track the fibers, such as FACT (fiber assignment by continuous tracking) [39], To track the fiber, as shown in Figure 3.10, we need to generate a continuous tensor field first, and then the tensor field can be simplified to a vector field defined by the first eigenvector. The fiber tracking begins with the definition of initial tracking points, which are usually defined by specifying one or more regions of interest (ROI). And then the ends of each discrete ellipsoids can be connected into an extended object, depicting the trajectory of a large fiber tract.

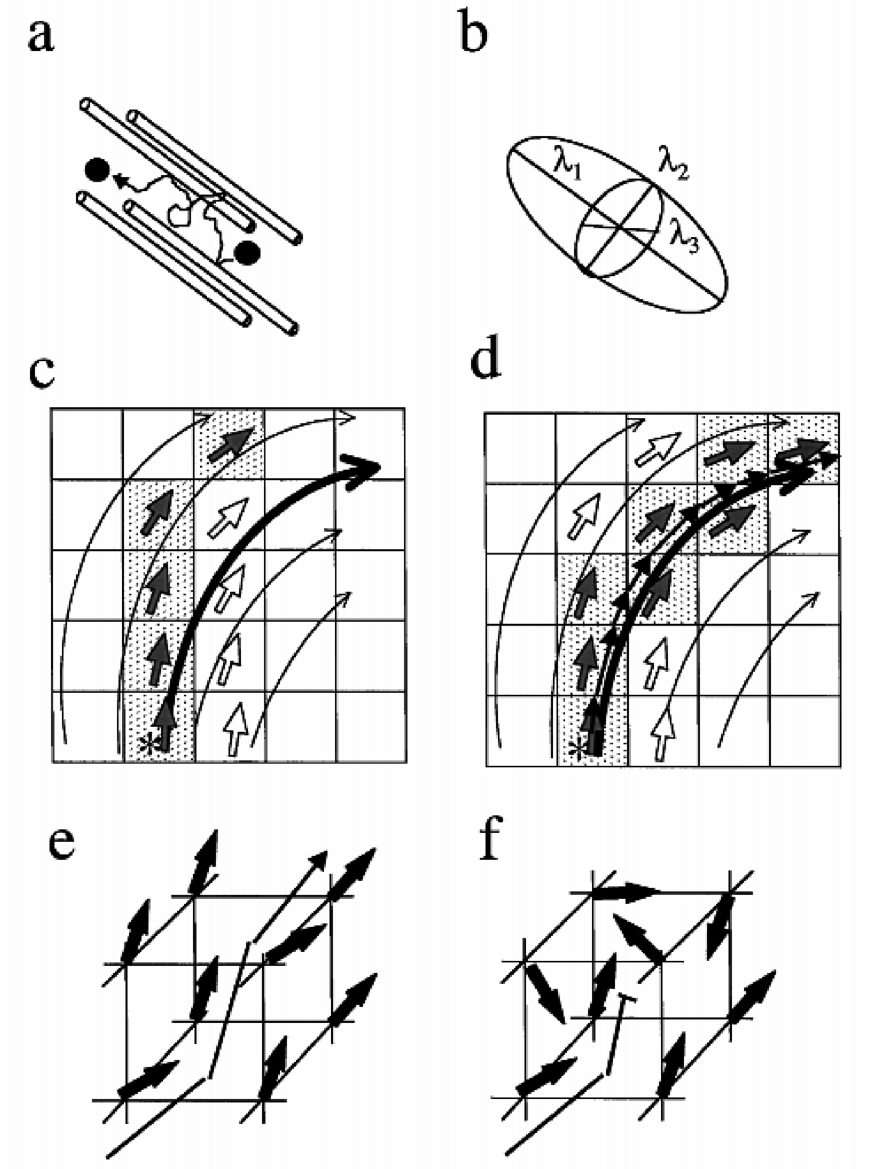

Figure 3.10: Principle of fiber tracking. (a) Schematic view of restricted water diffusion (solid sphere) in an environment with strongly aligned fibers (depicted by bars). The diffusion properties can be fully described by an ellipsoid (b) with three principal axes (λ_1, λ_2, and λ_3) of which the orientation of the main axis represents the average fiber direction. Once this direction is determined in each voxel, tracking can be performed by using either a discrete (c) or a continuous (d) number field. The actual fibers are indicated by curved arrows, and the average fiber directions in the voxel are displayed as open arrows. The connected voxel resulting from tracking are shaded, using dots. The discrete approach leads to deviation from the actual fiber to be tracked (c), whereas the continuous approach succeeds as indicated by the train of solid arrows (d). A 3D axon projection can be tracked as long as nearby vectors are strongly aligned (e). When vector orientation becomes random, the tracking is ended (f) [39].

References

[1] A. Einstein, "Über die von der molekularkinetischen theorie der wärme geforderte bewegung von in ruhenden flüssigkeiten suspendierten teilchen," *Annalen der Physik*, vol. 322, no. 8, p. 549–560, 1905. 04367.

[2] *MRI from Picture to Proton.* Cambridge University Press, 2007. 00306.

[3] E. Hahn, "Spin echoes," *Physical Review*, vol. 80, pp. 580–594, Nov. 1950. 04291.

[4] E. O. Stejskal and J. E. Tanner, "Spin diffusion measurements: Spin echoes in the presence of a time-dependent field gradient," *The Journal of Chemical Physics*, vol. 42, p. 288, Jan. 1965. 05424.

[5] D. Lebihan and E. Breton, "{Imagerie de Diffusion In Vivo par Résonance Magnétique Nucléaire.}," *XXX CR Académie des Sciences de Paris*, vol. 301, pp. 1109–1112, 1985. 00000.

[6] R. Turner, D. Le Bihan, and A. S. Chesnick, "Echo-planar imaging of diffusion and perfusion," *Magnetic resonance in medicine: official journal of the Society of Magnetic Resonance in Medicine / Society of Magnetic Resonance in Medicine*, vol. 19, pp. 247–253, June 1991. 00111.

[7] D. A. Porter and R. M. Heidemann, "High resolution diffusion-weighted imaging using readout-segmented echo-planar imaging, parallel imaging and a two-dimensional navigator-based reacquisition," *Magnetic Resonance in Medicine*, vol. 62, no. 2, p. 468–475, 2009. Cited by 0039.

[8] H. Y. Carr, "Steady-state free precession in nuclear magnetic resonance," *Physical Review*, vol. 112, pp. 1693–1701, Dec. 1958. 00328.

[9] R. Freeman and H. Hill, "Phase and intensity anomalies in fourier transform NMR," *Journal of Magnetic Resonance (1969)*, vol. 4, pp. 366–383, June 1971. 00268.

[10] W. S. Hinshaw, "Image formation by nuclear magnetic resonance: The sensitive-point method," *Journal of Applied Physics*, vol. 47, p. 3709, Aug. 1976. 00293.

[11] R. Kaiser, E. Bartholdi, and R. R. Ernst, "Diffusion and field-gradient effects in NMR fourier spectroscopy," *The Journal of Chemical Physics*, vol. 60, pp. 2966–2979, Apr. 1974. Cited by 0150.

[12] D. Le Bihan, “Intravoxel incoherent motion imaging using steady-state free precession,” *Magnetic Resonance in Medicine*, vol. 7, no. 3, p. 346–351, 1988. Cited by 0124.

[13] D. L. Bihan, R. Turner, and J. R. Macfall, “Effects of intravoxel incoherent motions (IVIM) in steady-state free precession (SSFP) imaging: application to molecular diffusion imaging,” *Magnetic Resonance in Medicine*, vol. 10, no. 3, p. 324–337, 1989. Cited by 0104.

[14] K.-D. Merboldt, W. Hänicke, M. L. Gyngell, J. Frahm, and H. Bruhn, “The influence of flow and motion in MRI of diffusion using a modified CE-FAST sequence,” *Magnetic Resonance in Medicine*, vol. 12, no. 2, p. 198–208, 1989. Cited by 0028.

[15] K.-D. Merboldt, H. Bruhn, J. Frahm, M. L. Gyngell, W. Hänicke, and M. Deimling, “MRI of “diffusion” in the human brain: New results using a modified CE-FAST sequence,” *Magnetic Resonance in Medicine*, vol. 9, no. 3, p. 423–429, 1989. Cited by 0061.

[16] S. Patz and R. C. Hawkes, “The application of steady-state free precession to the study of very slow fluid flow,” *Magnetic resonance in medicine: official journal of the Society of Magnetic Resonance in Medicine / Society of Magnetic Resonance in Medicine*, vol. 3, pp. 140–145, Feb. 1986. Cited by 0064.

[17] E. X. Wu and R. B. Buxton, “Effect of diffusion on the steady-state magnetization with pulsed field gradients,” *Journal of Magnetic Resonance (1969)*, vol. 90, pp. 243–253, Nov. 1990. Cited by 0057.

[18] R. B. Buxton, “The diffusion sensitivity of fast steady-state free precession imaging,” *Magnetic Resonance in Medicine*, vol. 29, no. 2, p. 235–243, 1993. Cited by 0078.

[19] J. A. McNab, S. Jbabdi, S. C. L. Deoni, G. Douaud, T. E. J. Behrens, and K. L. Miller, “High resolution diffusion-weighted imaging in fixed human brain using diffusion-weighted steady state free precession,” *NeuroImage*, vol. 46, pp. 775–785, July 2009. Cited by 0047.

[20] J. A. McNab and K. L. Miller, “Steady-state diffusion-weighted imaging: theory, acquisition and analysis,” *NMR in biomedicine*, vol. 23, pp. 781–793, Aug. 2010. PMID: 20886565.

[21] O. Bieri, C. Ganter, and K. Scheffler, "Quantitative in vivo diffusion imaging of cartilage using double echo steady-state free precession," *Magnetic resonance in medicine: official journal of the Society of Magnetic Resonance in Medicine / Society of Magnetic Resonance in Medicine*, vol. 68, pp. 720–729, Sept. 2012. Cited by 0007.

[22] D. Le Bihan and H. Johansen-Berg, "Diffusion MRI at 25: Exploring brain tissue structure and function," *NeuroImage*, vol. 61, pp. 324–341, June 2012. 00044.

[23] C. T. Moonen, J. Pekar, M. H. de Vleeschouwer, P. van Gelderen, P. C. van Zijl, and D. DesPres, "Restricted and anisotropic displacement of water in healthy cat brain and in stroke studied by NMR diffusion imaging," *Magnetic resonance in medicine: official journal of the Society of Magnetic Resonance in Medicine / Society of Magnetic Resonance in Medicine*, vol. 19, pp. 327–332, June 1991. 00119.

[24] D. Le Bihan, R. Turner, and P. Douek, "Is water diffusion restricted in human brain white matter? an echo-planar NMR imaging study," *Neuroreport*, vol. 4, pp. 887–890, July 1993. 00116.

[25] T. Niendorf, R. M. Dijkhuizen, D. G. Norris, M. van Lookeren Campagne, and K. Nicolay, "Biexponential diffusion attenuation in various states of brain tissue: implications for diffusion-weighted imaging," *Magnetic resonance in medicine: official journal of the Society of Magnetic Resonance in Medicine / Society of Magnetic Resonance in Medicine*, vol. 36, pp. 847–857, Dec. 1996. 00402.

[26] D. Le Bihan, E. Breton, D. Lallemand, M. L. Aubin, J. Vignaud, and M. Laval-Jeantet, "Separation of diffusion and perfusion in intravoxel incoherent motion MR imaging," *Radiology*, vol. 168, pp. 497–505, Aug. 1988. 00000.

[27] M. Maeda, Y. Kawamura, Y. Tamagawa, T. Matsuda, S. Itoh, H. Kimura, T. Iwasaki, N. Hayashi, K. Yamamoto, and Y. Ishii, "Intravoxel incoherent motion (IVIM) MRI in intracranial, extraaxial tumors and cysts," *Journal of computer assisted tomography*, vol. 16, pp. 514–518, Aug. 1992. PMID: 1629406.

[28] K. Kono, Y. Inoue, K. Nakayama, M. Shakudo, M. Morino, K. Ohata, K. Wakasa, and R. Yamada, "The role of diffusion-weighted imaging in patients with brain tumors," *AJNR. American journal of neuroradiology*, vol. 22, pp. 1081–1088, July 2001. PMID: 11415902.

[29] B. J. Hayempour, S. E. Rushing, and A. Alavi, “The role of neuroimaging in assessing neuropsychological deficits following traumatic brain injury,” *The Journal of psychiatry & law*, vol. 39, no. 4, pp. 537–566, 2011. 00004.

[30] B. J. Hayempour, S. Cohen, and A. Newberg, “Brain disorders: Evaluation by radiological techniques and nuclear medicine of the primitive major neuropsychiatric disorders,” *Journal of Alzheimer’s disease & Parkinsonism*, vol. 3, June 2013. PMID: 24040576.

[31] K. M. Bennett, K. M. Schmainda, R. T. Bennett, D. B. Rowe, H. Lu, and J. S. Hyde, “Characterization of continuously distributed cortical water diffusion rates with a stretched-exponential model,” *Magnetic resonance in medicine: official journal of the Society of Magnetic Resonance in Medicine / Society of Magnetic Resonance in Medicine*, vol. 50, pp. 727–734, Oct. 2003. Cited by 0096.

[32] K. M. Bennett, J. S. Hyde, and K. M. Schmainda, “Water diffusion heterogeneity index in the human brain is insensitive to the orientation of applied magnetic field gradients,” *Magnetic resonance in medicine: official journal of the Society of Magnetic Resonance in Medicine / Society of Magnetic Resonance in Medicine*, vol. 56, pp. 235–239, Aug. 2006. Cited by 0028.

[33] J. H. Jensen, J. A. Helpern, A. Ramani, H. Lu, and K. Kaczynski, “Diffusional kurtosis imaging: the quantification of non-gaussian water diffusion by means of magnetic resonance imaging,” *Magnetic resonance in medicine: official journal of the Society of Magnetic Resonance in Medicine / Society of Magnetic Resonance in Medicine*, vol. 53, pp. 1432–1440, June 2005. Cited by 0292.

[34] X. Yan, M. Zhou, L. Ying, D. Yin, M. Fan, G. Yang, Y. Zhou, F. Song, and D. Xu, “Evaluation of optimized b-value sampling schemas for diffusion kurtosis imaging with an application to stroke patient data,” *Computerized medical imaging and graphics: the official journal of the Computerized Medical Imaging Society*, vol. 37, pp. 272–280, June 2013. 00000.

[35] L. N. Mazzoni, S. Lucarini, S. Chiti, S. Busoni, C. Gori, and I. Menchi, “Diffusion-weighted signal models in healthy and cancerous peripheral prostate tissues: Comparison of outcomes obtained at different b-values,” *Journal of magnetic resonance imaging: JMRI*, May 2013. 00000.

[36] P. Mukherjee, J. I. Berman, S. W. Chung, C. P. Hess, and R. G. Henry, “Diffusion tensor MR imaging and fiber tractography: Theoretic underpinnings,” *American Journal of Neuroradiology*, vol. 29, pp. 632–641, Apr. 2008. Cited by 0130.

[37] P. J. Basser, J. Mattiello, and D. LeBihan, “MR diffusion tensor spectroscopy and imaging.,” *Biophysical Journal*, vol. 66, pp. 259–267, Jan. 1994. Cited by 2802.

[38] C. Pierpaoli, P. Jezzard, P. J. Basser, A. Barnett, and G. Di Chiro, “Diffusion tensor MR imaging of the human brain,” *Radiology*, vol. 201, pp. 637–648, Dec. 1996. Cited by 1738.

[39] S. Mori, B. J. Crain, V. P. Chacko, and P. C. van Zijl, “Three-dimensional tracking of axonal projections in the brain by magnetic resonance imaging,” *Annals of neurology*, vol. 45, pp. 265–269, Feb. 1999. Cited by 2024.

Chapter 4

Assessment of structural properties of facial skeletal muscle with diffusion MRI

4.1 Introduction

For a human being, the face has fundamental meaning. It is the unique external perceivable identity of his/her distinctive individual personality in daily contact with other persons and public authorities. At the same time it is the part of the body, where on a close area the most important sense organs are represented and where the mimic as an instrument for expression takes place. The facial muscle skeletal system consisting of the bony morphological fundamental and the functional soft tissue is therefore of major importance. This has to be considered for any surgical treatment to guarantee an optimal functional and esthetic outcome. Assessment of morphology and structure of facial skeletal muscle is one of the determinants of intervention planning in cranio-maxillo-facial (CMF) surgery.

Muscle architecture is the main determinant of the mechanical behavior of skeletal muscles. This architecture, which is defined as the arrangement of muscle fibers relative to the axis of force generation, is characterized by various parameters, including muscle length, fiber length, pennation angle, and physiological cross-sectional area.Accurate characterization of the arrangement of fascicles within muscle is essential for understanding muscle function and accurate simulation results. The excellent soft tissue contrast of MRI is perfectly suited to assess structural properties or morphology of muscle.

Diffusion Tensor Imaging (DTI) studies of skeletal muscle can provide information of muscle reference [1–3]. DTI [4] relies on the fact that the self diffusion of water in tissue is restricted by membranes and other cellular constituents, resulting in an apparent diffusion coefficient, which is lower than the free diffusion coefficient and is orientation-dependent for elongated structures. By measuring diffusion in six or more non collinear directions, this diffusion can be described using a tensor model. The tensor has three eigenvalues, which describe the magnitude of the diffusion coefficient in three orthogonal directions, and three eigenvectors, specifying those directions. The eigenvector corresponding to the largest eigenvalue is coincident with the longitudinal axis of the cell, and by following the direction of greatest diffusion , the local fiber trajectories can be reconstructed. These indices of micro structure, along with the ability to track fibers and visualize fiber sheet direction, provide an unprecedented opportunity to noninvasive study muscle structure–function relationships under rest and exercise conditions.

Several investigators have proven the feasibility of using diffusion tensor imaging (DTI) to show that the principle eigenvalue extracted from the diffusion tensor is aligned with the direction of fascicles within a muscle [5–14]. Multiple studies have investigated the possibility of applying DTI to segment different anatomical structures using the diffusion properties [15]. However, there are a number of practical complications to performing DTI in facial muscle. These include the short transverse relaxation time constant (T2) of muscle (~35ms, at 1.5T) [16], and its low fractional anisotropy value (FA, ~0.2 - ~0.4), thin thickness of facial muscles, subject motion during the long DTI acquisition time, and strong susceptibility changes around the muscle tissue make the adoption of conventional EPI-based diffusion weighted imaging challenging.

In this study, different techniques, diffusion weighted single shot Echo Planar Imaging (SS-EPI), diffusion weighted Readout-Segmented EPI (RS-EPI) [17,18], and diffusion weighted double echo steady state free precession sequence (DW-DESS) [19], were used and compared to visualize the facial muscle fiber tracking.

4.2 Materials and Methods

4.2.1 Imaging Techniques

As introduced in 3.3.3.1, SS-EPI is well established as the method of choice for diffusion weighted imaging and therefore for DTI. This is due to its low sensitivity to the motion induced phase errors that occur during diffusion sensitization of the MR signal. However, SS-EPI is prone to artifacts related to susceptibility changes at tissue interfaces and has a limited spatial resolution due to T2* relaxation [20]. Parallel imaging can be used to improve the image quality of SS-EPI acquisitions [21, 22], but there are still significant limitations, particularly at higher field strength.

The image quality of SS-EPI is generally impaired by significant geometric distortions, intravoxel dephasing, blurring, and poor spatial resolution, which can reduce DWI's ability to accurately depict the muscle fiber tractography. An additional technique that can be used with non - linear phase correction is RS-EPI . Following an initial description by Robson et. al. 1997 [23], the method, which was introduced in 3.3.3.3, was further developed in subsequent work to include k-space readout segmentation, 2D navigator correction, parallel imaging and navigator based reacquisition [18]. This approach can produce high resolution diffusion weighted images with a robust correction for motion induced phase errors.

DW-SSFP [24–30] accumulates signal from multiple echoes over several TRs yielding a strong sensitivity to diffusion with short gradient durations and imaging times. In addition to that, Bieri et. al. introduced a diffusion weighted double echo steady state free precession sequence (DW-DESS) [19], (as introduced in chapter 3), which is relaxation independent, for fast high-resolution in vivo quantitative DWI. It can offer strong diffusion sensitivity in combination with short echo times and overcomes problems with T2 relaxation related signal loss present on muscle tissue.

4.2.2 Image Acquisition

Experiments with SS-EPI were performed on a 1.5 T whole body system (Siemens Healthcare, Erlangen, Germany), for both ex vivo pig and in vivo human calf scans. For the scans on pork, data were acquired according to a 64 directions, 4slices, b-values : 0, 500 s/mm^2, 2mm X 2mm X 2mm isotropic voxel size, TR / TE = 5000 / 58 ms, with 8 averages protocol. The scan lasted 43 minutes 35 seconds. For the invivo experiments, we scanned the calf of one healthy volunteer. Data were acquired according to a 64 directions, 48 slices, b-values : 0, 500 s/mm^2, 3.8mm X 3.8mm X 2mm voxel size, TR / TE = 5100 / 59 ms, with 1 averages protocol. The scan lasted 5 minutes 47 seconds.

The RS-EPI sequence was tested first by applying it to human calf invivo scan. The data were acquired according to a 30 directions, 60 slices, b-values: 0, 500 s/mm^2, 2.4mm isotropic voxel size, TR / TE = 5800 / 48 ms protocol. The acquisition time as 20 minutes 23 seconds. For the facial muscle invivo scan, in addition to a standard 12 channel head coil, a 4cm diameter loop coil was placed on the right cheek to locally increase SNR. Data were acquired according to a 20 directions, 40slices, b-values: 0, 500 s/mm^2, 3mm isotropic voxel size, TR / TE = 3700 / 47 ms protocol.

A DW-DESS sequence applying diffusion weighting sequentially in three orthogonal directions was modified, optimized, tested and evaluated for invivo diffusion weighted imaging of the facial muscles. First, in vitro experiments were carried out on a spherical phantom and invivo 3D examinations of facial muscles on a 3T scanner. To optimize the protocol the following parameters were varied: fat suppression technique, spatial resolution, used RF receive coil (12channel head coil vs. loop surface coil), amplitude of the diffusion weighting gradient, direction of the applied diffusion weighting gradients (phase, read, and slice), receive bandwidth, and flip angle. These 3D acquisitions suffered from numerous artifacts due to motion and susceptibility changes. Then, 2D in vitro and invivo scans were performed with a 32-channels receive coil on a 3T clinical MRI system. Images were acquired in either coronal or sagittal orientation, yielding 0.7 mm in-plane resolution (240 x 320 image encoding matrix) and 1 mm in-plane resolution (176 x 256 image encoding matrix). Diffusion weighting was applied in read, phase and slice encoding direction.

4.2.3 Data Processing and Visualization

Prior to further analysis, all the diffusion-weighted images were co-registered using SPM8 (Wellcome Trust Centre for Neuroimaging, London, UK) in Matlab (The Math Works Inc., Natick, MA, USA). All the muscle fibers were tracked by the Diffusion Toolkit software package (Massachusetts General Hospital, USA).

The fiber tracking algorithm we used here is FACT, which was introduced in section 3.5.4.

4.3 Results

The images of the pork acquired by SS-EPI at b = 0 $s/mm^2$are presented in Figure 4.1 (a), and with the resulting fiber tracking of the corresponding DTI analysis of the 64 direction data set are shown in Figure. 4.1(b). The colors of the fiber tracks are encoded in this way: red indicates directions in right to left or left to right; green indicates directions in posterior to anterior or from anterior to posterior; and blue indicates directions in foot-to-head direction or vice versa.

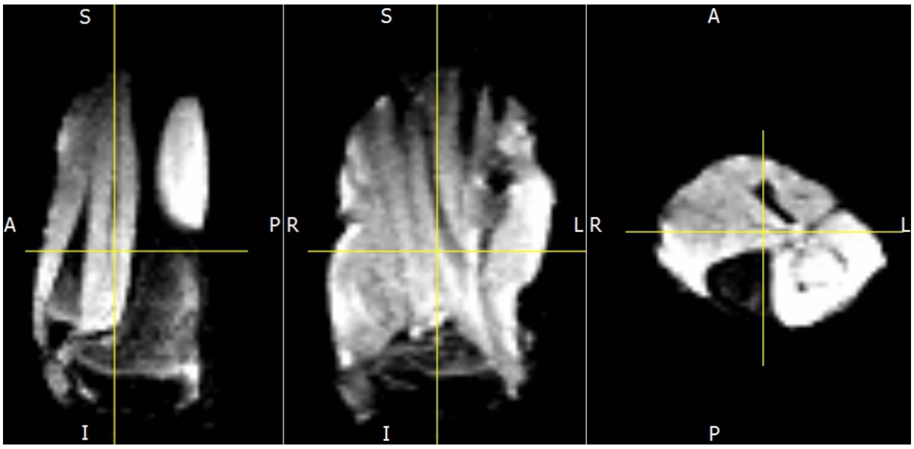

(a)

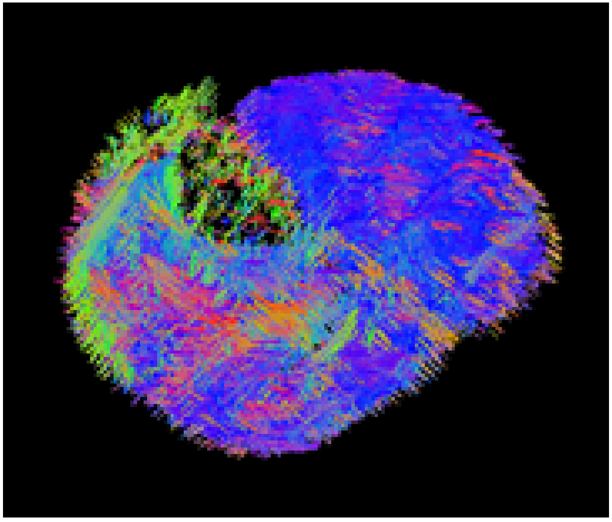

(b)

Figure 4.1: Images at b=0s/mm^2 in three orientations: right - left, posterior - anterior, and Superior - inferior (a) and visualization of fiber tracking of pork using SS-EPI

Figure 4.2 (a) and Figure 4.3 (a) directly compares images at b = 0 s/mm^2 obtained by using SS-EPI and RS-EPI in calf muscle. The SS-EPI acquisition suffers from significant image blurring and the images acquired with RS-EPI shows reduced blurring. The resulting fiber track from SS-EPI is displayed in Figure 4.2 (b), and the fiber track accuracy is lower than the resulting fiber tracking from RS-EPI images showed in Figure 4.2 (b).

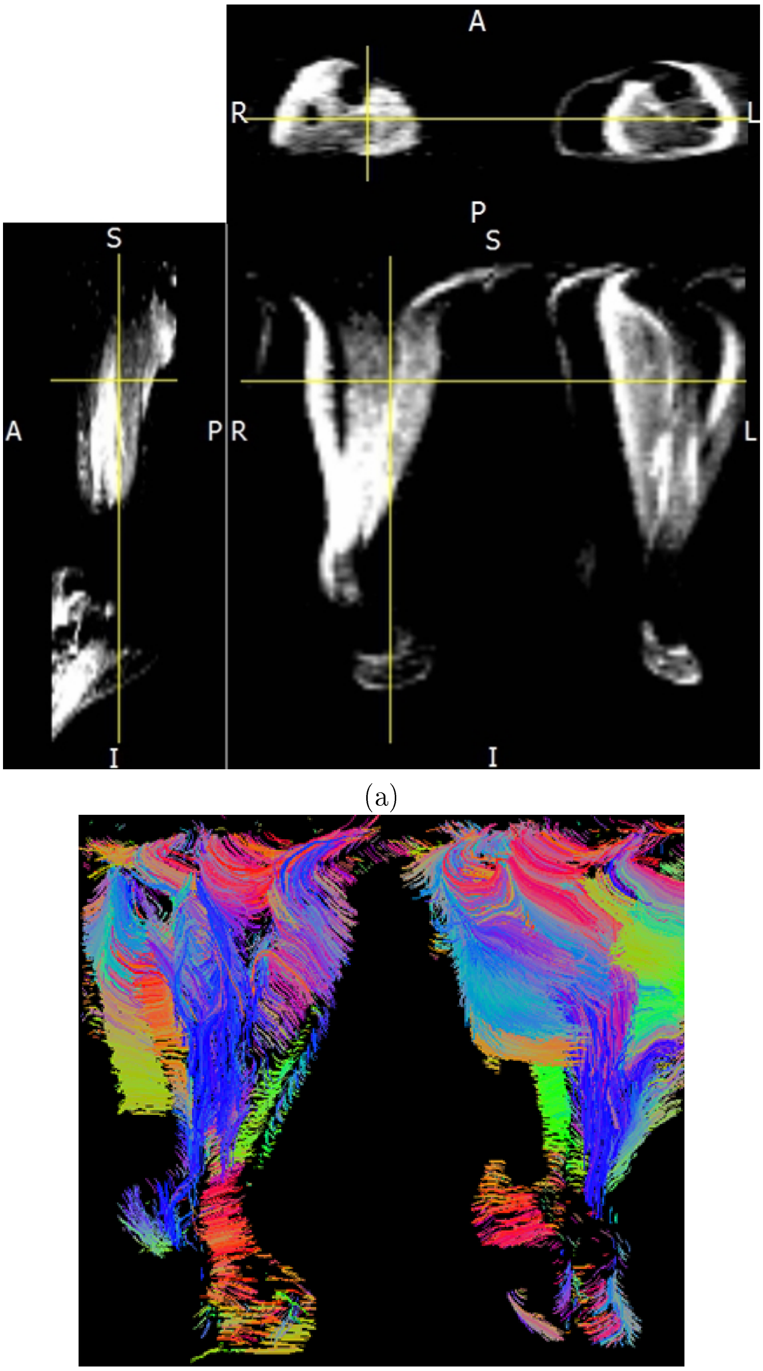

(a)

(b)

Figure 4.2: Images at b=$0s/mm^2$ in three orientations: right - left, posterior - anterior, and Superior - inferior (a) and visualization of fiber tracking of human calf with the used of SS-EPI

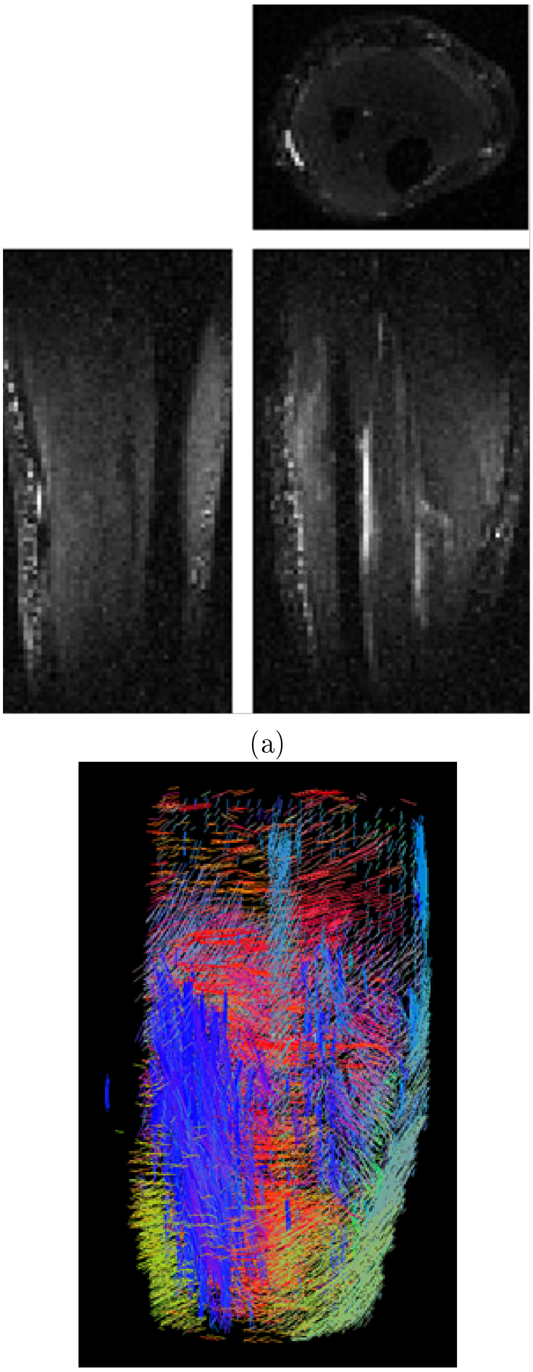

(a)

(b)

Figure 4.3: Images of b = 0 s/mm^2in calf (a) and visualization of calf muscle fiber tracking with the use of RS-EPI sequence

The high effective bandwidth in phase-encoding direction of the RS-EPI sequence enabled diffusion-weighted MR imaging of facial muscles, which is commonly hindered by artifacts and signal voids due to strong susceptibility changes and short T2 of muscle tissue. The images of the facial muscle acquired by RS-EPI at b = 0 $s/mm^2$are presented in Figure 4.4. Figure 4.5 (b) shows obtained muscle fiber tracks crossing the ROI defined in Figure 4.5 (a). Two facial muscle groups can be observed: Buccinator muscle fibers running in anterior-posterior direction are shown in red whereas fibers running in superior-inferior displayed in green are part of the Masseter muscle.

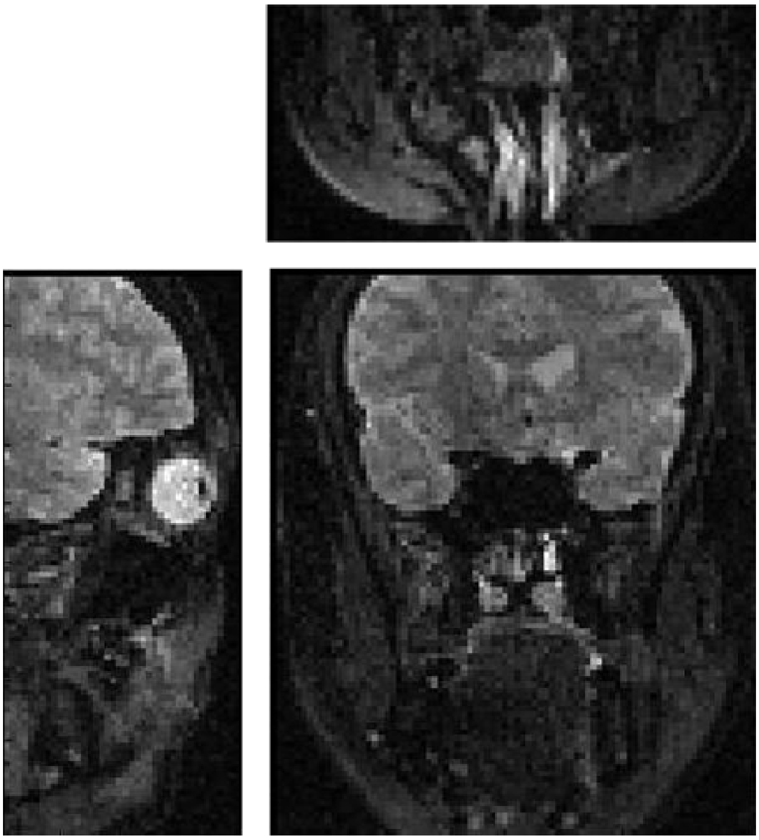

Figure 4.4: Images of b = 0 $s/mm^2$of facial muscle in three orientations: right - left, posterior - anterior, and Superior - inferior, using RS-EPI

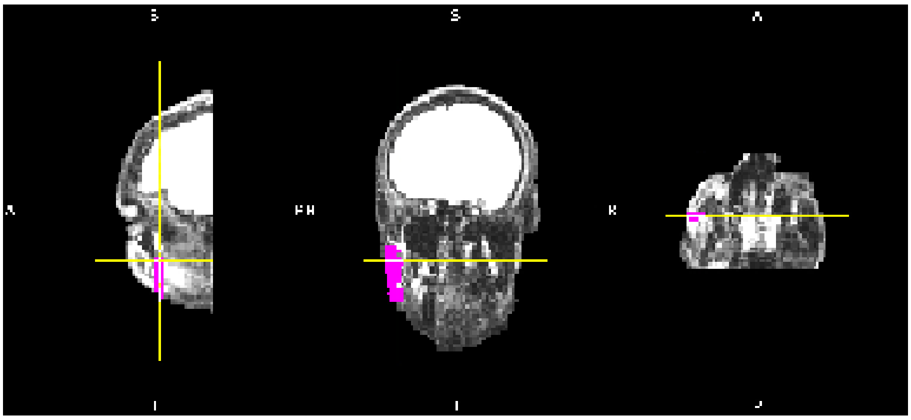

(a)

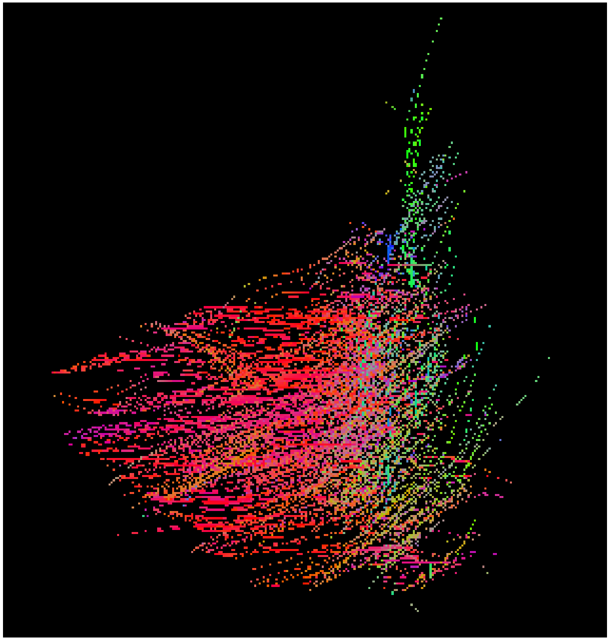

(b)

Figure 4.5: Facial muscle fiber tracking with RS-EPI (b) through the roi presented in (a)

The ADC maps acquired by DW-DESS are shown in Figure 4.6 and Figure 4.7. As a reference, a region-of-interest from the corpus callosum was chosen, in which the derived ADC values were much higher in the phase and read directions than those in the slice direction, which correctly reflects the nerve anatomy. For the facial muscle fiber, in the coronal images, the ADC values were much higher in the slice direction than those in the phase and read directions. In the sagittal images, the ADC values were higher in the phase and read directions than those in the slice direction. These results indicated that the interested muscle fiber group went from the lower left to top right direction. These results are in agreement with the anatomy of facial muscles.

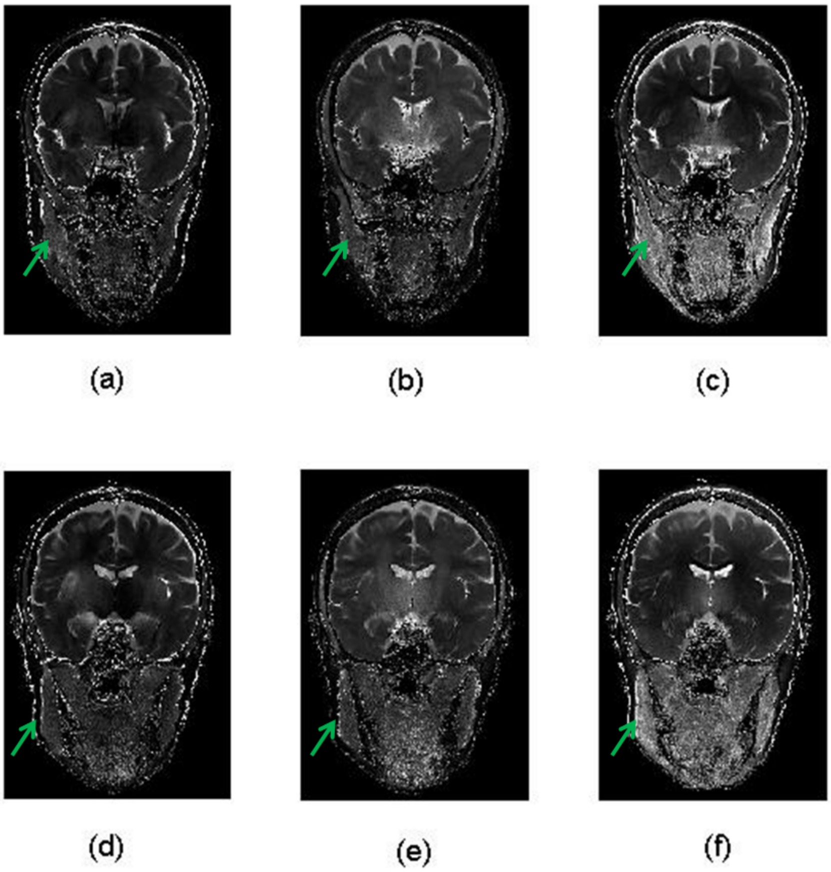

Figure 4.6: ADC maps of 2 slices of coronal images: (a, d) diffusion gradient in the phase direction, (b, e) diffusion gradient in the read direction, (c, f) diffusion gradient in the slice direction. The Green arrows point to the interested muscle group.

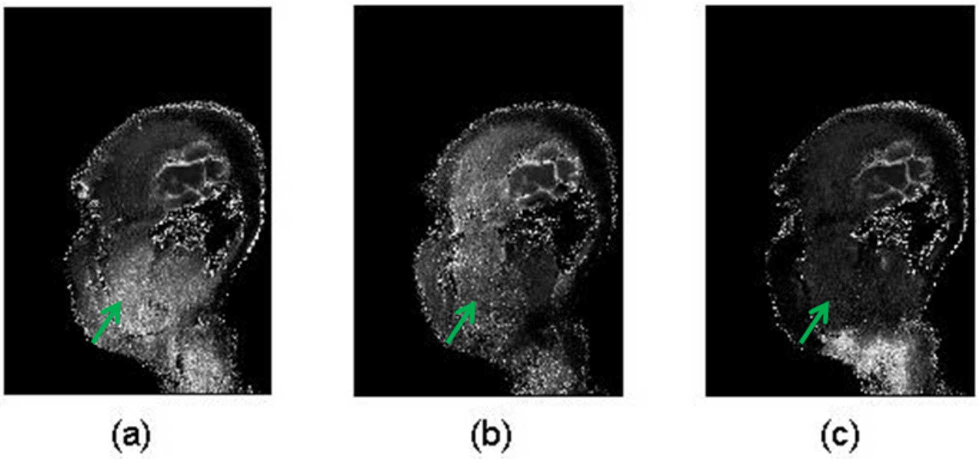

Figure 4.7: ADC maps of sagittal images: (a) diffusion gradient in the phase direction, (b) diffusion gradient in the read direction, (c) diffusion gradient in the slice direction. The Green arrows point to the interested muscle group.

4.4 Discussion and Conclusion

The noninvasive character of DWI allows in vivo investigation of muscle fiber structure. However, DWI in skeletal muscle is complicated by the short T_2 relaxation times [16], and lower water proton density compared with that of brain tissue [31]. In this study, three different diffusion weighted imaging techniques were compared for fiber tracking of facial muscles.

The sequence most frequently used for DWI is SS-EPI. It is fast and insensitive to motion, but the disadvantages of SS-EPI are a limited spatial resolution and distortions caused by susceptibility changes. Distortion in EPI is driven by the slow traversal through k-space along the phase-encoding direction [20]. The performance of EPI based imaging methods can be improved when the distortions are compensated by the use of alternate trajectories in k-space, such as RS-EPI [17, 32], particularly when combined with parallel imaging [18]. By using RS-EPI, the short readout length of the individual adjacent EPI segments results in a much shorter echo-spacing, hence less distortion and a corresponding reduction in TE when the same resolution and phase-encoding partial Fourier factors are used. The RS-EPI protocols in this study used a full k-space acquisition, giving a shorter TE than SS-EPI, and resulting in better SNR. At higher spatial resolutions, there are further benefits by using the RS-EPI sequence because the increased resolution in the readout direction can be achieved by increasing the number of shots without changing the echo-spacing, but the scan time is considerably prolonged. In contrast, with the SS-EPI sequence, a longer echo-spacing is required when the resolution in the readout direction is increased, so that the duration of the EPI readout and consequently the TE increase more rapidly with increasing spatial resolution. In this study, the additional use of small surface coil leads to sufficient SNR for reliable tracking of the muscle fibers. Resulting facial muscle fiber tracks generated by RS-EPI are in good agreement with the muscular anatomy.

However, DTI fiber tracking in small muscles remains challenging because of partial volume effects. Increasing the spatial resolution of the skeletal facial muscle can be hindered by the inherently low SNR because of short T_2 time. Compared to diffusion weighted EPI techniques, DW-DESS [33, 34] is relaxation independent, with higher resolution and considerably higher SNR . By using this approach, the image can achieve a higher resolution, giving more information of the small facial muscle groups.

In addition, the choice of b-values is very important in DWI [19, 35, 36]. The use of a high b value would be advantageous to generate large intensity differences between different diffusion weighted gradients, which can reduce the error in the fiber tracking. But, the use of higher b-values results in a longer echo-time and lower SNR, because the SNR is affected by the different TEs for the various b-values, as well as increased T2 relaxation leaded by increased TE. Therefore, an optimal b value should be found to leverage the effects of potentially improved fiber tracking accuracy at higher b values with decreased accuracy as a result of noise and acquisition time. Saupe et. al [10] suggested the use of 625 s/mm^2 in calf muscle at 1.5T. But in this study, the target tissue is the facial skeletal muscle, which has less thickness and stronger susceptibility changes, so a maximum b-value of 500 s/mm^2 was used in both SS-EPI and RS-EPI sequences to balance the problems.

In conclusion, it was demonstrated that the RS-EPI seems to be a promising approach for visualization of muscle fiber orientation. At the same time, the use of DW-DESS can provide additional information about small muscle groups due to its higher spatial resolution.

References

[1] M. Froeling, A. J. Nederveen, D. F. Heijtel, A. Lataster, C. Bos, K. Nicolay, M. Maas, M. R. Drost, and G. J. Strijkers, “Diffusion-tensor MRI reveals the complex muscle architecture of the human forearm,” *Journal of Magnetic Resonance Imaging*, vol. 36, no. 1, p. 237–248, 2012. Cited by 0005.

[2] M. Froeling, A. J. Nederveen, K. Nicolay, and G. J. Strijkers, “DTI of human skeletal muscle: the effects of diffusion encoding parameters, signal-to-noise ratio and t2 on tensor indices and fiber tracts,” *NMR in biomedicine*, May 2013. 00000.

[3] M. Scheel, P. von Roth, T. Winkler, A. Arampatzis, T. Prokscha, B. Hamm, and G. Diederichs, “Fiber type characterization in skeletal muscle by diffusion tensor imaging,” *NMR in biomedicine*, vol. 26, pp. 1220–1224, Oct. 2013. 00000.

[4] P. J. Basser and D. K. Jones, “Diffusion-tensor MRI: theory, experimental design and data analysis – a technical review,” *NMR in Biomedicine*, vol. 15, no. 7-8, p. 456–467, 2002. 00769.

[5] D. A. Lansdown, Z. Ding, M. Wadington, J. L. Hornberger, and B. M. Damon, “Quantitative diffusion tensor MRI-based fiber tracking of human skeletal muscle,” *Journal of Applied Physiology*, vol. 103, pp. 673–681, Aug. 2007. Cited by 0074.

[6] U. Sinha and L. Yao, “In vivo diffusion tensor imaging of human calf muscle,” *Journal of Magnetic Resonance Imaging*, vol. 15, no. 1, p. 87–95, 2002. Cited by 0061.

[7] J. F. Budzik, V. Le Thuc, X. Demondion, M. Morel, D. Chechin, and A. Cotten, “In vivo MR tractography of thigh muscles using diffusion imaging: initial results,” *European radiology*, vol. 17, pp. 3079–3085, Dec. 2007. 00043.

[8] J. F. Deux, P. Malzy, N. Paragios, G. Bassez, A. Luciani, P. Zerbib, F. Roudot-Thoraval, A. Vignaud, H. Kobeiter, and A. Rahmouni, “Assessment of calf muscle contraction by diffusion tensor imaging,” *European radiology*, vol. 18, pp. 2303–2310, Oct. 2008. 00029.

[9] E. Kermarrec, J.-F. Budzik, C. Khalil, V. Le Thuc, C. Hancart-Destee, and A. Cotten, “In vivo diffusion tensor imaging and tractography of human thigh muscles in healthy subjects,” *AJR. American journal of roentgenology*, vol. 195, pp. W352–356, Nov. 2010. 00008.

[10] N. Saupe, L. M. White, J. Stainsby, G. Tomlinson, and M. S. Sussman, “Diffusion tensor imaging and fiber tractography of skeletal muscle: optimization of b value for imaging at 1.5 t,” *AJR. American journal of roentgenology*, vol. 192, pp. W282–290, June 2009. 00017.

[11] B. M. Damon, Z. Ding, A. W. Anderson, A. S. Freyer, and J. C. Gore, “Validation of diffusion tensor MRI-based muscle fiber tracking,” *Magnetic Resonance in Medicine*, vol. 48, no. 1, p. 97–104, 2002. Cited by 0116.

[12] A. A. Holmes, D. Scollan, and R. L. Winslow, “Direct histological validation of diffusion tensor MRI in formaldehyde-fixed myocardium,” *Magnetic Resonance in Medicine*, vol. 44, no. 1, p. 157–161, 2000. 00139.

[13] N. J. Olsen, J. Qi, and J. H. Park, “Imaging and skeletal muscle disease,” *Current Rheumatology Reports*, vol. 7, pp. 106–114, Apr. 2005. 00012.

[14] C. J. Galbán, S. Maderwald, K. Uffmann, A. d. Greiff, and M. E. Ladd, “Diffusive sensitivity to muscle architecture: a magnetic resonance diffusion tensor imaging study of the human calf,” *European Journal of Applied Physiology*, vol. 93, pp. 253–262, Dec. 2004. Cited by 0000.

[15] C. J. Galbán, S. Maderwald, K. Uffmann, A. de Greiff, and M. E. Ladd, “Diffusive sensitivity to muscle architecture: a magnetic resonance diffusion tensor imaging study of the human calf,” *European journal of applied physiology*, vol. 93, pp. 253–262, Dec. 2004. Cited by 0000.

[16] P. S. Belton, R. R. Jackson, and K. J. Packer, “Pulsed NMR studies of water in striated muscle. i. transverse nuclear spin relaxation times and freezing effects,” *Biochimica et biophysica acta*, vol. 286, pp. 16–25, Nov. 1972. 00208.

[17] S. J. Holdsworth, S. Skare, R. D. Newbould, R. Guzmann, N. H. Blevins, and R. Bammer, “Readout-segmented EPI for rapid high resolution diffusion imaging at 3 t,” *European journal of radiology*, vol. 65, pp. 36–46, Jan. 2008. 00000.

[18] D. A. Porter and R. M. Heidemann, “High resolution diffusion-weighted imaging using readout-segmented echo-planar imaging, parallel imaging and a two-dimensional navigator-based reacquisition,” *Magnetic Resonance in Medicine*, vol. 62, no. 2, p. 468–475, 2009. Cited by 0039.

[19] O. Bieri, C. Ganter, and K. Scheffler, “Quantitative in vivo diffusion imaging of cartilage using double echo steady-state free precession,” *Magnetic resonance in*

medicine: official journal of the Society of Magnetic Resonance in Medicine / Society of Magnetic Resonance in Medicine, vol. 68, pp. 720–729, Sept. 2012. Cited by 0007.

[20] F. Farzaneh, S. J. Riederer, and N. J. Pelc, "Analysis of t2 limitations and off-resonance effects on spatial resolution and artifacts in echo-planar imaging," *Magnetic resonance in medicine: official journal of the Society of Magnetic Resonance in Medicine / Society of Magnetic Resonance in Medicine*, vol. 14, pp. 123–139, Apr. 1990. 00252.

[21] M. A. Griswold, P. M. Jakob, Q. Chen, J. W. Goldfarb, W. J. Manning, R. R. Edelman, and D. K. Sodickson, "Resolution enhancement in single-shot imaging using simultaneous acquisition of spatial harmonics (SMASH)," *Magnetic resonance in medicine: official journal of the Society of Magnetic Resonance in Medicine / Society of Magnetic Resonance in Medicine*, vol. 41, pp. 1236–1245, June 1999. 00137.

[22] R. Bammer, S. L. Keeling, M. Augustin, K. P. Pruessmann, R. Wolf, R. Stollberger, H. P. Hartung, and F. Fazekas, "Improved diffusion-weighted single-shot echo-planar imaging (EPI) in stroke using sensitivity encoding (SENSE)," *Magnetic resonance in medicine: official journal of the Society of Magnetic Resonance in Medicine / Society of Magnetic Resonance in Medicine*, vol. 46, pp. 548–554, Sept. 2001. 00240.

[23] M. D. Robson, A. W. Anderson, and J. C. Gore, "Diffusion-weighted multiple shot echo planar imaging of humans without navigation," *Magnetic Resonance in Medicine*, vol. 38, no. 1, p. 82–88, 1997. Cited by 0034.

[24] R. Kaiser, E. Bartholdi, and R. R. Ernst, "Diffusion and field-gradient effects in NMR fourier spectroscopy," *The Journal of Chemical Physics*, vol. 60, pp. 2966–2979, Apr. 1974. Cited by 0150.

[25] D. Le Bihan, "Intravoxel incoherent motion imaging using steady-state free precession," *Magnetic Resonance in Medicine*, vol. 7, no. 3, p. 346–351, 1988. Cited by 0124.

[26] D. L. Bihan, R. Turner, and J. R. Macfall, "Effects of intravoxel incoherent motions (IVIM) in steady-state free precession (SSFP) imaging: application to molecular diffusion imaging," *Magnetic Resonance in Medicine*, vol. 10, no. 3, p. 324–337, 1989. Cited by 0104.

[27] K.-D. Merboldt, W. Hänicke, M. L. Gyngell, J. Frahm, and H. Bruhn, “The influence of flow and motion in MRI of diffusion using a modified CE-FAST sequence,” *Magnetic Resonance in Medicine*, vol. 12, no. 2, p. 198–208, 1989. Cited by 0028.

[28] K.-D. Merboldt, H. Bruhn, J. Frahm, M. L. Gyngell, W. Hänicke, and M. Deimling, “MRI of “diffusion” in the human brain: New results using a modified CE-FAST sequence,” *Magnetic Resonance in Medicine*, vol. 9, no. 3, p. 423–429, 1989. Cited by 0061.

[29] S. Patz and R. C. Hawkes, “The application of steady-state free precession to the study of very slow fluid flow,” *Magnetic resonance in medicine: official journal of the Society of Magnetic Resonance in Medicine / Society of Magnetic Resonance in Medicine*, vol. 3, pp. 140–145, Feb. 1986. Cited by 0064.

[30] R. B. Buxton, “The diffusion sensitivity of fast steady-state free precession imaging,” *Magnetic Resonance in Medicine*, vol. 29, no. 2, p. 235–243, 1993. Cited by 0078.

[31] T. Ichikawa, H. Haradome, J. Hachiya, T. Nitatori, and T. Araki, “Diffusion-weighted MR imaging with a single-shot echoplanar sequence: detection and characterization of focal hepatic lesions,” *AJR. American journal of roentgenology*, vol. 170, pp. 397–402, Feb. 1998. 00356.

[32] K. W. Yeom, S. J. Holdsworth, A. T. Van, M. Iv, S. Skare, R. M. Lober, and R. Bammer, “Comparison of readout-segmented echo-planar imaging (EPI) and single-shot EPI in clinical application of diffusion-weighted imaging of the pediatric brain,” *American Journal of Roentgenology*, vol. 200, pp. W437–W443, May 2013. 00000.

[33] H. Bruder, H. Fischer, R. Graumann, and M. Deimling, “A new steady-state imaging sequence for simultaneous acquisition of two MR images with clearly different contrasts,” *Magnetic Resonance in Medicine*, vol. 7, no. 1, p. 35–42, 1988. 00062.

[34] T. W. Redpath and R. A. Jones, “FADE–A new fast imaging sequence,” *Magnetic Resonance in Medicine*, vol. 6, no. 2, p. 224–234, 1988. 00043.

[35] N. Saupe, L. M. White, M. S. Sussman, A. Kassner, G. Tomlinson, and M. D. Noseworthy, “Diffusion tensor magnetic resonance imaging of the human calf: comparison between 1.5 t and 3.0 t-preliminary results,” *Investigative radiology*, vol. 43, pp. 612–618, Sept. 2008. 00023.

[36] M. W. A. Caan, H. Khedoe, D. H. J. Poot, A. den Dekker, S. Olabarriaga, K. Grimbergen, L. van Vliet, and F. Vos, “Estimation of diffusion properties in crossing fiber bundles,” *IEEE Transactions on Medical Imaging*, vol. 29, no. 8, pp. 1504–1515, 2010. 00011.

Chapter 5

Comparison of Different Models for Analysis of Renal Diffusion Imaging

5.1 Introduction

Diffusion-weighted MR imaging has been used to characterize abdominal organs and renal lesions [1–11]. With diffusion weighting, the signal in the abdomen deviates from a mono-exponential form. This behavior reflects microscopic tissue properties such as water compartmentalization and diffusional restrictions. This phenomenon, also known as non-Gaussian diffusion, constitutes a novel contrast mechanism in human abdominal imaging. Compared to the standard mono-exponential approach to analyze diffusion weighted MRI data, the application of more complex models can result in valuable additional insight into pathological processes.

Conventional diffusion imaging is a sensitive technique. Different tissue microstructures may give the same apparent diffusion coefficient (ADC). Taking anisotropy into account by measuring the diffusion tensor, provides metrics, like fractional anisotropy, that may differentiate between tissues with equal ADC values. With reliable metrics of non-Gaussian, the diffusion measurements can be improved even further. Bennett [12–14], LeBihan [15], and Jensen et.al. [16, 17] have shown that non-Gaussian diffusion provides clinically useful information.

Different models (mono-exponential model, stretched-exponential model [12–14], and bi-exponential model [15, 18–20]) may incorporate explicitly effects such as compartmentalization, extracellular tortuosity, permeability or exchange rates, axon size distribution, fiber orientation, and possibly fanning and bending of fiber tracts. Analyzing diffusion measurements in light of such models, therefore, may give unique insight into tissue micro-structure. A possible drawback with this approach is that the models may need a large number of adjustable parameters to fit the measurements well. To resolve all parameters, one needs long-lasting and accurate measurements. This is feasible ex-vivo or in animal studies. In clinical imaging, however, there are limitations posed by imaging gradient strength, and acquisition time.

In this study, we focus on these models. The applicability of such models is not limited to specific geometries and therefore, they can be used for neuro imaging as well as body imaging [21]. They use a limited number of free parameters. This allows reliable measurements to be carried out in the amount of time available for clinical protocols. Furthermore, the data processing, which often involves nonlinear optimization, is quicker and problems can be reduced if we use a smaller number of fitted parameters. Parameter maps that measure non-Gaussian diffusion are used as a new image contrast. The drawback of this approach is that the model parameters are not directly related to tissue properties. However, non-Gaussian diffusion can be correlated to pathology, thereby increasing diagnostic specificity. Three-parameter models are particularly appealing. The reason is that the purpose of each parameter is obvious: One parameter measures the diffusivity, one quantifies the amount of non-Gaussian and one measures the signal intensity in the absence of diffusion weighting. Furthermore, a low number of fitted parameters may be desirable, because over-parametrization can cause numerical instability and ill-defined parameters.

Measuring non-Gaussian diffusion with good precision requires more b-values and better signal-to-noise ratio (SNR) than those used to determine ADC. The precision of the estimates will be increased if we measure the signal for a wide range of b-values. Therefore, to fully exploit non-Gaussian diffusion as a novel imaging contrast, we need models that describe the signal well at high b - values. It is also desirable to have models for which the parameter estimates do not depend strongly upon the experimental set-up, i.e., the number of b-values and the maximum b-value.

This retrospective study compares results from mono-exponential, stretched-exponential, kurtosis model and bi-exponential models, which were applied to analyze renal diffusion imaging data sets. Reference data for each model were obtained from healthy subjects, and then the reference model parameters were compared to the results from selected renal pathologies, including cysts, renal cell carcinomas (RCC), and angiomyolipoma (AML).

5.2 Materials and Methods

5.2.1 Study population

Volunteers with healthy kidneys were included: 4 men, 6 women, age 27 - 42 (30±6) years. A retrospective study was performed to identify the selected renal lesions on abdominal MRI from February 2010 to November 2012 (during which time DWI was acquired in clinical abdominal MRI examinations). Data from 19 patients were obtained retrospectively in this study to give a comparison to the healthy volunteers: 10 men, 9 women, age from 30 to 85 years old with of 55 years and standard deviation of 18 years, 12 RCCs, 8 Cysts, and 2 AMLs were included.

5.2.2 Image Acquisition

Data of healthy volunteers were acquired on a Siemens 1.5 T Avanto system (Siemens, Erlangen, Germany) and patients data were acquired on Siemens 1.5 T systems (Avanto, Espree, and Symphony, Siemens, Erlangen, Germany). A body coil was used for transmit. We measured 8 b-values of 0, 10, 40, 70, 120, 250, 450, and 700 s/mm^2. Three orthogonal gradient directions were used (Right–Left, Anterior–Posterior, and Feet–Head). For each b-value, four averages were acquired. We used a single-shot spin-echo diffusion-weighted sequence with a 90 excitation pulse and echo-planar read-out with free breathing. The echo time was 65 ms, and the repetition time was 3700 ms. We measured 23 transverse slices of 6 mm slice thickness and a slice gap with distance factor of 22%. The field-of-vie acquisition matrix was196 $\times$ 152, giving approximately 2.4x2.2x6.0 mm^3 voxel size. To avoid phase errors from flow and motion, the images were magnitude reconstructed. Parallel imaging was used with an acceleration factor of 2. And we also used the partial Fourier of 6/8 . The Acquisition time was 5 min 38s. This protocol was implanted in the clinical routine for abdominal MRI examination.

5.2.3 Data Analysis

For the processing of the data, we needed the thermal noise level. This quantity was estimated by calculating the signal in several ROIs in air.

Four different models shown below (as introduced in Chapter 3) were fitted to five volunteers data and six representative patients data on a pixel by pixel basis in matlab (The Math Works Inc., Natick, MA, USA). Pixel intensities below the previously-defined noise threshold where excluded from the fitting and a Levenberg-Marquardt minimum least squares nonlinear fitting algorithm was used to fit the following models: mono-exponential diffusion model with the ADC. The stretched exponential model including the stretching parameter α, that defines the deviation of the signal decay from a mono-exponential and the distributed diffusion coefficient DDC.The Kurtosis model described results in an apparent diffusion coefficient D_{app} and the mean diffusional kurtosis K_{app}. The bi-exponential model consists of the perfusion fraction f, the diffusion coefficient D_1 and the pseudo-diffusion coefficient D_2.

$$S(b) = S(0) \times exp\{-b \times ADC\} \tag{5.1}$$

$$S(b) = S(0) \times exp\{-(b \times DDC)^{\alpha}\} \tag{5.2}$$

$$S(b) = S(0) \times exp\left\{-bD_{app} + \frac{1}{6}b^2 D_{app}^2 K_{app}\right\} \tag{5.3}$$

$$S = S(0) \times \{f \cdot exp(-b \cdot D_2) + (1-f) \cdot exp(-b \cdot D_1)\} \tag{5.4}$$

In the bi-exponential model, we first used high b-value points (from 250 s/mm^2) where were considered to have no perfusion effect anymore in kidney [22–24] to fit the diffusion coefficient D_1 with mono-exponential model. Then we used this fitted diffusion coefficient D_1 as a fixed value in the bi-exponential model to fit the rest 3 parameters as described by Le Bihan et al. [25].

Because the highest b-value is 700 s/mm^2 is not efficient for kurtosis analysis [26–28], then we used three models (the mono-exponential model, stretched-exponential model and bi-exponential model) to evaluate all the volunteers data.

5.2.4 ROI positioning

In the study of the first five volunteers and six patients, one ROI in medulla, one ROI in cortex in each kidney of the five volunteers were drawn. In the patients maps, ROIs in five cysts, three RCCs, and one AML were also drawn. In the study of all the volunteers and all the patients, the ROIs were drawn over the whole kidney in healthy volunteers data, and ROIs in the patients were drawn over the whole kidney and the lesions by using Matlab (The Math Works Inc., Natick, MA, USA). To compare the difference, the ROIs in the patients only cover the lesions were also drawn. This task was done manually by using MITK Workbench (Division of Medical and Biological Informatics of DKFZ). All the patient ROIs were located in the diffusion weighted images, while the T1-weighted, or T2-weighted images were viewed separately, and then controlled in the ADC maps. In the control group, the ROIs were placed in the b = 0 s/mm^2 images, while the ADC maps were viewed separately.

5.2.5 Statistical analysis

All the statistical analysis of the data is performed using Matlab.

Histogram analysis is used to provide not only mean ADC, α, and perfusion fraction values, but also ADC, α, and perfusion fraction histogram skewness, which reflect the distribution of each parameter value and therefore take tissue heterogeneity into account.

Student t-tests are applied to detect differences in tissue types for ADC, α, and perfusion fraction values. Significance tests are two-sided, and $P<0.05$ is chosen as the criterion for significance. Correlation coefficients are calculated to study the correlation of these parameters: ADC, α, and perfusion fraction.

All the uncertainties are given in terms of the standard deviation (mean ± std).

5.3 Results

Figure 5.1 shows the signal intensity of the roi in one healthy volunteer for three different model overlaid. The logarithmic vertical scale for the signal intensity displays a mono-exponential curve as a straight line (blue). The stretched-exponential curve displays a deviation from a straight line at all b-values, while the bi-exponential curve at low b-values which indicates a second component in the data.

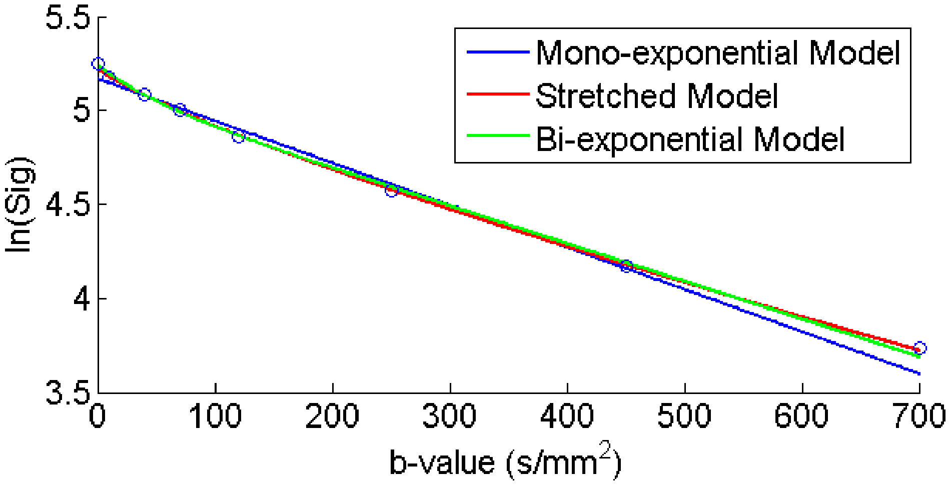

Figure 5.1: Corresponding graphs of the logarithmic scale for the signal intensity of one healthy subject with mono-exponential model, stretched-exponential model, and bi-exponential model overlaid.

Pixel wise fitted results from the kidneys of one healthy volunteer and two patients are shown in Figure 5.2. All models allow a differentiation of the pathologies from healthy tissues. Figure 5.3 presents the average values of the fitted results of the five healthy subjects, as well as ROI-based values from the focal pathologies present in the patients. Both the stretched exponential model and the kurtosis model provided solid fit results for the parameters α and Kapp, respectively. While the cysts are characterized by α close to 1, solid kidney lesions show a clear deviation from mono-exponential behavior with α values around 0.5. This deviation from Gaussian diffusion is even more pronounced in the kurtosis maps, where both RCC and AML lesions can be clearly differentiated from healthy parenchyma by their higher Kapp, which is consistent with reduced diffusivity in the tumor due to high cellular density. Moreover, in the bi-exponential model, the perfusion fraction of cysts is close to 0, while both RCC and AML lesions show considerable deviation from mono-exponential behavior indicating increased perfusion.

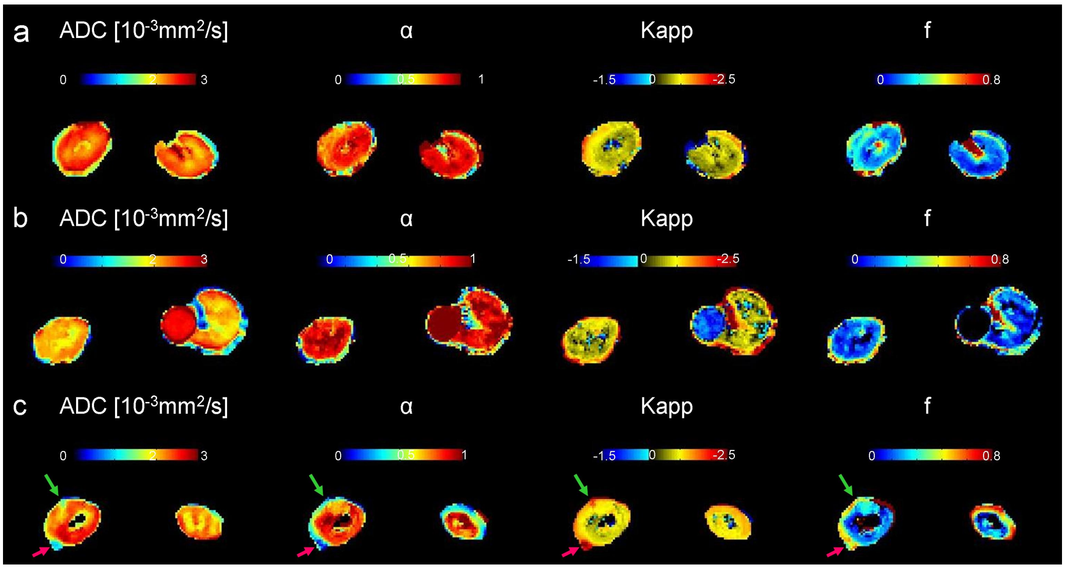
a
ADC [10-3mm2/s]
0
3
α
0
1
Kapp
-1.5
0
2.5
f
0
0.8
b
ADC [10-3mm2/s]
0
2
3
α
0
0.5
1
Kapp
-1.5
0
2.5
f
0
0.8
c
ADC [10-3mm2/s]
0
3
α
0
1
Kapp
-1.5
0
2.5
f
0
0.8

Figure 5.2: Fit maps of one healthy volunteer (a), one patient with one cyst (b), and one patient with two RCCs (c).

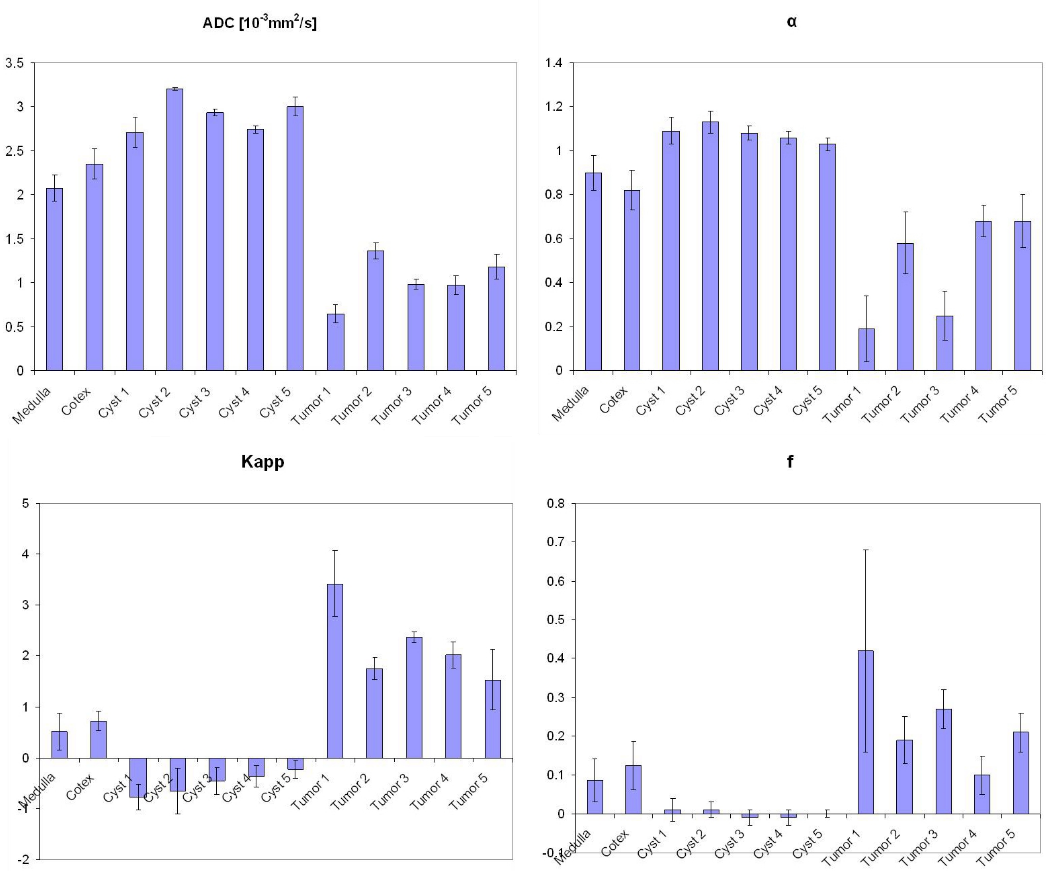

Figure 5.3: Bar charts of the mean values for five healthy volunteers, five cysts, three RCC lesions, and one AML.

Characteristic normalized histograms of ADC, α , and perfusion fraction for one AML, one RCC, one Cyst, and one healthy volunteer are shown in Figure 5.4. For the ADC values, the histogram of cyst shifts down from very large ADC values to lower values in control group, and the ADC histograms of AML and RCC have a broader range than control group due to the tissue heterogeneity. The histogram of the stretched parameter α for RCC give a wide distribution than all the rest groups. And the perfusion fraction histogram of cyst is much acuter than the other groups.

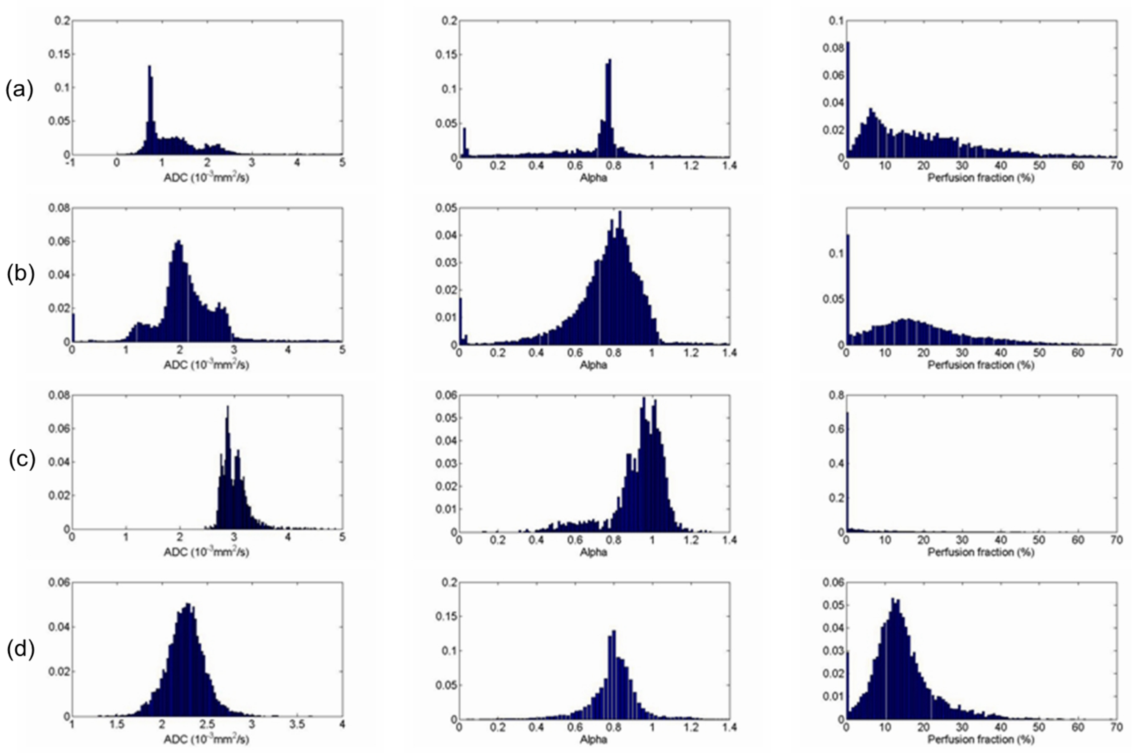

Figure 5.4: Normalized histograms of ADC, α , and perfusion fraction for one AML (a), one RCC (b), one Cyst (c), and one healthy volunteer (d).

The average ROI size of all included lesions is 11215±11708 pixels. The average size of AMLs is 2576±3500 pixel; the average size of RCCs is 11215±25260 pixel; and the average size of cysts is 800±948 pixel. The average ROI size of control group is 6931±1682 pixel.

The parameters of the ADC, α , and perfusion fraction for the whole group of patients with AML, RCC, and cyst and the whole control group are shown in Table 5.1. The solid lesion (AML and RCC) gives a lower ADC and α value than the control group, and the cyst shows a higher ADC and α values than the control group. While the solid lesion holds higher perfusion fraction than the control group, and the cyst is with a lower perfusion fraction than the control group.

Parameter	AML	RCC	Cyst	Control Group
ADC ($10^{-3}mm^2/s$)	1.62±0.54	1.67±0.44	2.86±0.27	2.25±0.09
α	0.70±0.06	0.73±0.04	0.84±0.09	0.80±0.03
Perfusion fraction (%)	19.8±1.8	16.4±4.3	11.0±6.3	15.0±1.9

Table 5.1: Diffusion parameters of renal lesions and control group

According to the Student t-test, the ADC, and α values of RCC are significantly lower than those of Cyst ($p<0.05$) and control group ($p<0.05$). The ADC value of cyst is significantly higher than that of control group ($p<0.05$). The perfusion fraction of cyst is significantly lower than that of AML ($p<0.05$) and RCC ($p<0.05$).

The skewness for all the groups are shown in Table 5.2. According to the Student t-test, the α values of RCC is significantly higher than that of AML ($p<0.05$), which give additional information of comparing AML and RCC. Interestingly, as shown in Figure 5.4, the α values of RCC is more broadly distributed than the other groups.

Skewness	AML	RCC	Cyst	Control Group
ADC	0.95±1.30	1.67±0.44	0.14±0.93	0.27±1.32
α	-0.58±0.14	-1.43±1.14	-0.74±0.74	-1.24±0.82
Perfusion fraction	0.18±0.60	0.98±0.56	1.00±1.18	1.88±0.30

Table 5.2: Skewness of each parameters for different renal lesions and control group.

In the analysis of all whole lesions and control group, as shown in Figure 5.5, ADC values for the RCC and AML have a heavier tail than those of the cyst and control group; α values for the AML and cyst have a heavier tail than those of the RCC and control group; and compare to the control group, the perfusion fractions for AML, RCC and cyst all have broader distribution. Because of the tumor heterogeneity, single whole lesion statistical analysis should be performed with care.

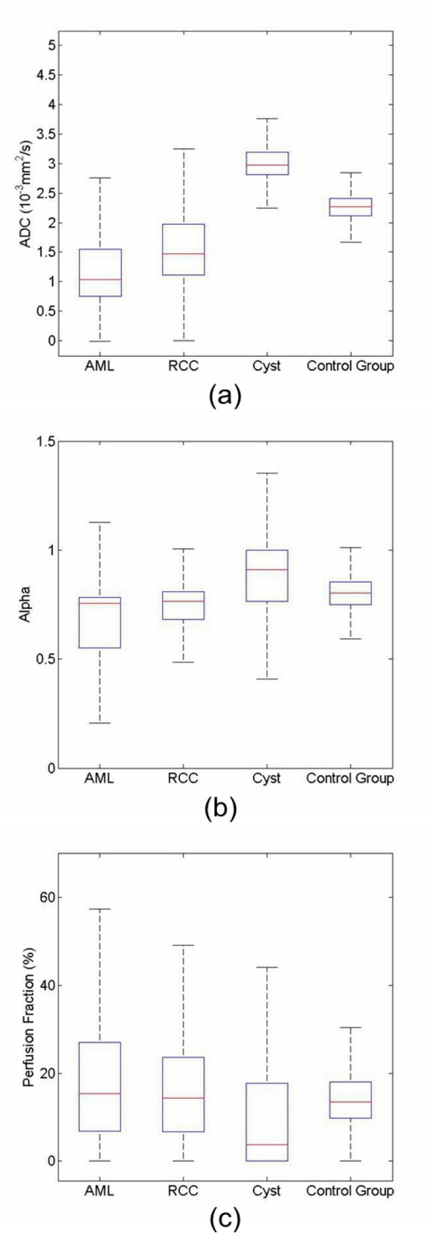

(a)

(b)

(c)

Figure 5.5: Box plots of ADC (a), α (b), and perfusion fraction (c) for different subgroups

As shown in Figure 5.6, we find a correlation between ADC and α values with a correlation coefficient of 0.1364, and between ADC and perfusion fraction with a correlation coefficient of 0.1481; while there is a weak correlation between α and perfusion fraction with a correlation coefficient of -0.5523. Therefore, the α values might be changed independently of the type of lesions either due to the diffusion characteristics. The α value and perfusion fraction may give additional information for distinguishing different lesion types.

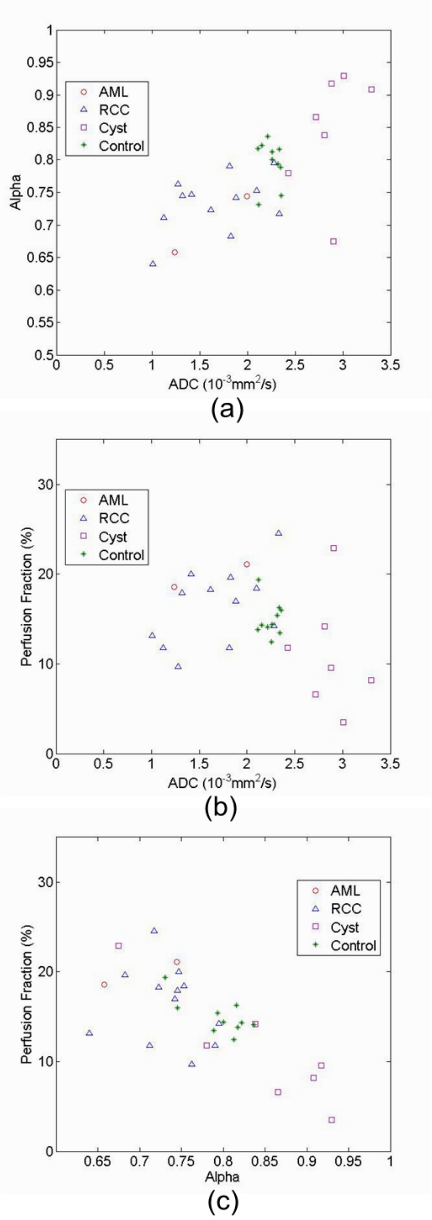

Figure 5.6: Scatter plots of all included patients (AML - read dots, RCC - blue triangles, and cyst - purple squares) and control group (green stars): (a) ADC against α, (b) ADC against perfusion fraction, (c) perfusion fraction against α.

5.4 Discussion and Conclusion

Diffusion weighted imaging has become a valuable tool to detect renal lesions [29–31]. In this retrospective study, besides the mono-exponential model, three different non-Gaussian diffusion models were used and compared to study renal diffusion imaging.

Because of the strong effect of breathing on kidney displacement between expiration and deep inspiration [32], an important issue of DWI in kidney is the choice of the most suitable respiration technique to acquire the images. Acquiring data with breath holding is effective in minimizing motion, but severely restricts the length of each scan, which may lead to a relatively low SNR, as well as for some patients, it is challenging to perform breath holding reliably. Navigator controlled DWI can be used to obtain thinner slices, but the acquisition time is considerably prolonged. However, patients often have irregular breathing that can decrease the time-efficiency of the acquisition, or even render the navigator regime unusable in some cases. But with the free breathing, thanks to continuous data acquisition, thin slices with many signal averages can be achieved to increase the SNR. While there are differences in the implementations of the three regimes from a patient's perspective, the derivation of parameters likely to be used in clinical interpretation and decision making does not clearly favor one method [33–36]. In this study, free breathing was chosen to obtain more averages to achieve better SNR.

In addition, when performing DW MRI with quantitative analysis of the models, attention has to be paid to the underlying b-values. So far, b-values from 0 to 1000 s/mm^2 have been used [2, 3, 37–40], whereby pseudo-diffusion due to IVIM can be excluded by using b-values higher than 250 s/mm^2 [22–24] .Therefore, in this study, we used the introduced multiple b-values, four values below and four above this threshold, with a maximum b value of $700 s/mm^2$.

The ADC values of AML and RCC are significantly lower than that of control group. This finding could be explained because of higher cellularity of these lesions, which restricts the motion of water molecules. The ADC value of cyst is significantly higher than the control group, which may be because of the cyst contains more liquid which has higher diffusion. In the stretched-exponential approach, the stretched parameter α value of RCC has no significant difference from that of AML, but the skewness of α value for RCC is significantly different from that for AML, which gives additional information about this two types of tumor. This skewness changes can also be seen in the histogram of AML has a heavier tail than that of RCC, this is may also because of the tissue heterogeneity. In the bi-exponential model, the perfusion fraction of cyst is significantly lower than that of AML and RCC, this can be explained that cyst has much lower perfusion and less restrict molecular diffusion.

Our data shows a broad distribution of ADC, α and perfusion fraction values in all renal lesions but a narrower distribution of control group as shown in Figure 5.5. This is agree with the histological findings in different lesions, such as solid lesion heterogeneity, and inflammations. And in this study, different pathologies show an overlap in all the parameter values, and no clear tend in the values of AML, RCC, cyst and control group.

There are some limitations in this study. The roi sizes of different type of lesions have a wide range: 101 - 5050 pixel in AML, 71 - 38397 pixel in RCC, 25-2521 pixel in cyst, and 4205 - 9780 pixel in control group. This may influence the calculated parameters. The spatial resolution is relatively low, which may lead to partial volume effects. Further more, our patient group is relatively small.

In conclusion, in this retrospective study, it demonstrates that quantification of renal DWI data by stretched-exponential model, diffusion kurtosis model and bi-exponential model can result in additional parameters, which enable a better characterization of different lesion types like cysts, RCCs, and AMLs. However, the particular application areas of the stretched-exponential model and the kurtosis model are still unclear. Therefore, further studies are needed to explore these open problems.

References

[1] C. L. Siegel, A. M. Aisen, J. H. Ellis, F. Londy, and T. L. Chenevert, "Feasibility of MR diffusion studies in the kidney," *Journal of magnetic resonance imaging: JMRI*, vol. 5, pp. 617–620, Oct. 1995. 00059.

[2] T. Namimoto, Y. Yamashita, K. Mitsuzaki, Y. Nakayama, Y. Tang, and M. Takahashi, "Measurement of the apparent diffusion coefficient in diffuse renal disease by diffusion-weighted echo-planar MR imaging," *Journal of Magnetic Resonance Imaging*, vol. 9, no. 6, p. 832–837, 1999. 00175.

[3] V. S. Lee, H. Rusinek, L. Bokacheva, A. J. Huang, N. Oesingmann, Q. Chen, M. Kaur, K. Prince, T. Song, E. L. Kramer, and E. F. Leonard, "Renal function measurements from MR renography and a simplified multicompartmental model," *American journal of physiology. Renal physiology*, vol. 292, pp. F1548–1559, May 2007. 00081.

[4] A. Qayyum, "Diffusion-weighted imaging in the abdomen and pelvis: concepts and applications," *Radiographics: a review publication of the Radiological Society of North America, Inc*, vol. 29, pp. 1797–1810, Oct. 2009. 00095.

[5] A. B. Rosenkrantz, M. Oei, J. S. Babb, B. E. Niver, and B. Taouli, "Diffusion-weighted imaging of the abdomen at 3.0 tesla: image quality and apparent diffusion coefficient reproducibility compared with 1.5 tesla," *Journal of magnetic resonance imaging: JMRI*, vol. 33, pp. 128–135, Jan. 2011. 00047.

[6] H. Chandarana, V. S. Lee, E. Hecht, B. Taouli, and E. E. Sigmund, "Comparison of biexponential and monoexponential model of diffusion weighted imaging in evaluation of renal lesions: Preliminary experience," *Investigative Radiology May 2011*, vol. 46, no. 5, pp. 285–291, 2011. 00053.

[7] C. Schmid-Tannwald, A. Oto, M. F. Reiser, and C. J. Zech, "Diffusion-weighted MRI of the abdomen: current value in clinical routine," *Journal of magnetic resonance imaging: JMRI*, vol. 37, pp. 35–47, Jan. 2013. 00002.

[8] S. M. Erturk, T. Ichikawa, E. Kaya, O. Yapici, A. Ozel, A. S. Mahmutoglu, and M. Basak, "Diffusion tensor imaging of cysts, hemangiomas, and metastases of the liver," *Acta radiologica (Stockholm, Sweden: 1987)*, Sept. 2013. 00000.

[9] D.-M. Koh and D. J. Collins, "Diffusion-weighted MRI in the body: Applications and challenges in oncology," Nov. 2012. 00000.

[10] A. C. Braithwaite, B. M. Dale, D. T. Boll, and E. M. Merkle, “Short- and midterm reproducibility of apparent diffusion coefficient measurements at 3.0-t diffusion-weighted imaging of the abdomen,” *Radiology*, vol. 250, pp. 459–465, Feb. 2009. 00000.

[11] T. Yoshikawa, H. Kawamitsu, D. G. Mitchell, Y. Ohno, Y. Ku, Y. Seo, M. Fujii, and K. Sugimura, “ADC measurement of abdominal organs and lesions using parallel imaging technique,” *AJR. American journal of roentgenology*, vol. 187, pp. 1521–1530, Dec. 2006. 00198.

[12] K. M. Bennett, K. M. Schmainda, R. T. Bennett, D. B. Rowe, H. Lu, and J. S. Hyde, “Characterization of continuously distributed cortical water diffusion rates with a stretched-exponential model,” *Magnetic resonance in medicine: official journal of the Society of Magnetic Resonance in Medicine / Society of Magnetic Resonance in Medicine*, vol. 50, pp. 727–734, Oct. 2003. Cited by 0096.

[13] K. M. Bennett, J. S. Hyde, S. D. Rand, R. Bennett, H. G. J. Krouwer, K. J. Rebro, and K. M. Schmainda, “Intravoxel distribution of DWI decay rates reveals c6 glioma invasion in rat brain,” *Magnetic resonance in medicine: official journal of the Society of Magnetic Resonance in Medicine / Society of Magnetic Resonance in Medicine*, vol. 52, pp. 994–1004, Nov. 2004. Cited by 0027.

[14] K. M. Bennett, J. S. Hyde, and K. M. Schmainda, “Water diffusion heterogeneity index in the human brain is insensitive to the orientation of applied magnetic field gradients,” *Magnetic resonance in medicine: official journal of the Society of Magnetic Resonance in Medicine / Society of Magnetic Resonance in Medicine*, vol. 56, pp. 235–239, Aug. 2006. Cited by 0028.

[15] D. Le Bihan, “Intravoxel incoherent motion perfusion MR imaging: a wake-up call,” *Radiology*, vol. 249, pp. 748–752, Dec. 2008. Cited by 0000.

[16] J. H. Jensen, J. A. Helpern, A. Ramani, H. Lu, and K. Kaczynski, “Diffusional kurtosis imaging: the quantification of non-gaussian water diffusion by means of magnetic resonance imaging,” *Magnetic resonance in medicine: official journal of the Society of Magnetic Resonance in Medicine / Society of Magnetic Resonance in Medicine*, vol. 53, pp. 1432–1440, June 2005. Cited by 0292.

[17] J. H. Jensen and J. A. Helpern, “MRI quantification of non-gaussian water diffusion by kurtosis analysis,” *NMR in biomedicine*, vol. 23, pp. 698–710, Aug. 2010. 00095.

[18] P. Eckerbom, P. Hansell, T. Bjerner, F. Palm, J. Weis, and P. Liss, "Intravoxel incoherent motion MR imaging of the kidney: pilot study," *Advances in experimental medicine and biology*, vol. 765, pp. 55–58, 2013. 00002.

[19] Y. Lu, J. F. A. Jansen, Y. Mazaheri, H. E. Stambuk, J. A. Koutcher, and A. Shukla-Dave, "Extension of the intravoxel incoherent motion model to non-gaussian diffusion in head and neck cancer," *Journal of magnetic resonance imaging: JMRI*, vol. 36, pp. 1088–1096, Nov. 2012. 00003.

[20] M. F. Müller, P. V. Prasad, and R. R. Edelman, "Can the IVIM model be used for renal perfusion imaging?," *European journal of radiology*, vol. 26, pp. 297–303, Feb. 1998. Cited by 0022.

[21] D.-M. Koh, D. J. Collins, and M. R. Orton, "Intravoxel incoherent motion in body diffusion-weighted MRI: reality and challenges," Nov. 2012. Cited by 0000.

[22] H. Wang, L. Cheng, X. Zhang, D. Wang, A. Guo, Y. Gao, and H. Ye, "Renal cell carcinoma: diffusion-weighted MR imaging for subtype differentiation at 3.0 t," *Radiology*, vol. 257, pp. 135–143, Oct. 2010. Cited by 0000.

[23] H. C. Thoeny and F. D. Keyzer, "Diffusion-weighted MR imaging of native and transplanted kidneys," *Radiology*, vol. 259, pp. 25–38, Apr. 2011. 00030.

[24] M. Freiman, S. D. Voss, R. V. Mulkern, J. M. Perez-Rossello, M. J. Callahan, and S. K. Warfield, "In vivo assessment of optimal b-value range for perfusion-insensitive apparent diffusion coefficient imaging," *Medical Physics*, vol. 39, pp. 4832–4839, Aug. 2012. 00003.

[25] D. Le Bihan, E. Breton, D. Lallemand, M. L. Aubin, J. Vignaud, and M. Laval-Jeantet, "Separation of diffusion and perfusion in intravoxel incoherent motion MR imaging," *Radiology*, vol. 168, pp. 497–505, Aug. 1988. 00000.

[26] X. Yan, M. Zhou, L. Ying, D. Yin, M. Fan, G. Yang, Y. Zhou, F. Song, and D. Xu, "Evaluation of optimized b-value sampling schemas for diffusion kurtosis imaging with an application to stroke patient data," *Computerized medical imaging and graphics: the official journal of the Computerized Medical Imaging Society*, vol. 37, pp. 272–280, June 2013. 00000.

[27] L. N. Mazzoni, S. Lucarini, S. Chiti, S. Busoni, C. Gori, and I. Menchi, "Diffusion-weighted signal models in healthy and cancerous peripheral prostate tissues: Com-

parison of outcomes obtained at different b-values," *Journal of magnetic resonance imaging: JMRI*, May 2013. 00000.

[28] A. B. Rosenkrantz, E. E. Sigmund, G. Johnson, J. S. Babb, T. C. Mussi, J. Melamed, S. S. Taneja, V. S. Lee, and J. H. Jensen, "Prostate cancer: Feasibility and preliminary experience of a diffusional kurtosis model for detection and assessment of aggressiveness of peripheral zone cancer," *Radiology*, vol. 264, pp. 126–135, July 2012. PMID: 22550312.

[29] J. Zhang, Y. M. Tehrani, L. Wang, N. M. Ishill, L. H. Schwartz, and H. Hricak, "Renal masses: Characterization with diffusion-weighted MR Imaging—A preliminary experience1," *Radiology*, vol. 247, pp. 458–464, May 2008. 00129.

[30] K. Sandrasegaran, C. P. Sundaram, R. Ramaswamy, F. M. Akisik, M. P. Rydberg, C. Lin, and A. M. Aisen, "Usefulness of diffusion-weighted imaging in the evaluation of renal masses," *American Journal of Roentgenology*, vol. 194, pp. 438–445, Feb. 2010. 00059.

[31] B. Taouli, R. K. Thakur, L. Mannelli, J. S. Babb, S. Kim, E. M. Hecht, V. S. Lee, and G. M. Israel, "Renal lesions: characterization with diffusion-weighted imaging versus contrast-enhanced MR imaging," *Radiology*, vol. 251, pp. 398–407, May 2009. Cited by 0116.

[32] L. H. Schwartz, J. Richaud, L. Buffat, E. Touboul, and M. Schlienger, "Kidney mobility during respiration," *Radiotherapy and Oncology*, vol. 32, pp. 84–86, July 1994. 00094.

[33] H. C. Thoeny, F. De Keyzer, R. H. Oyen, and R. R. Peeters, "Diffusion-weighted MR imaging of kidneys in healthy volunteers and patients with parenchymal diseases: initial experience," *Radiology*, vol. 235, pp. 911–917, June 2005. 00000.

[34] M. Notohamiprodjo, O. Dietrich, W. Horger, A. Horng, A. D. Helck, K. A. Herrmann, M. F. Reiser, and C. Glaser, "Diffusion tensor imaging (DTI) of the kidney at 3 tesla-feasibility, protocol evaluation and comparison to 1.5 tesla," *Investigative Radiology May 2010*, vol. 45, no. 5, pp. 245–254, 2010. 00035.

[35] N. P. Jerome, M. R. Orton, J. A. d'Arcy, D. J. Collins, D.-M. Koh, and M. O. Leach, "Comparison of free-breathing with navigator-controlled acquisition regimes in abdominal diffusion-weighted magnetic resonance images: Effect on ADC and IVIM statistics," *Journal of magnetic resonance imaging: JMRI*, Apr. 2013. 00000.

[36] T. C. Kwee, T. Takahara, I. Muro, M. V. Cauteren, Y. Imai, R. A. J. Nievelstein, W. P. T. M. Mali, and P. R. Luijten, "Apparent diffusion coefficient measurement in a moving phantom simulating linear respiratory motion," *Japanese Journal of Radiology*, vol. 28, pp. 578–583, Oct. 2010. 00001.

[37] J. L. Zhang, E. E. Sigmund, H. Rusinek, H. Chandarana, P. Storey, Q. Chen, and V. S. Lee, "Optimization of b-value sampling for diffusion-weighted imaging of the kidney," *Magnetic Resonance in Medicine*, vol. 67, no. 1, p. 89–97, 2012. 00017.

[38] Z. Koc and G. Erbay, "Optimal b value in diffusion-weighted imaging for differentiation of abdominal lesions," *Journal of Magnetic Resonance Imaging*, p. n/a–n/a, 2013. 00000.

[39] G. Erbay, Z. Koc, E. Karadeli, B. Kuzgunbay, M. R. Goren, and N. Bal, "Evaluation of malignant and benign renal lesions using diffusion-weighted MRI with multiple b values," *Acta radiologica (Stockholm, Sweden: 1987)*, vol. 53, pp. 359–365, Apr. 2012. 00003.

[40] B. Gürses, N. Tasdelen, F. Yencilek, N. O. Kılıckesmez, T. Alp, Z. Fırat, M. S. Albayrak, A. M. Uluğ, and A. N. Gürmen, "Diagnostic utility of DTI in prostate cancer," *European journal of radiology*, vol. 79, pp. 172–176, Aug. 2011. PMID: 20138721.

Chapter 6

Summary and Outlook

6.1 Summary

MR measurement of diffusion in tissue can provide unique biologically and clinically relevant information which is not available from other imaging methods. This information includes parameters that help characterize tissue microstructure.

The main goal of this thesis was to study the micro-structure of tissues using diffusion weighted magnetic resonance imaging, which has potential for clinical use.

This thesis was developed into two different directions. First is assessment of structural properties of facial skeletal muscle with diffusion MRI (Chapter 4). And the second part is to compare different diffusion models in renal diffusion imaging (Chapter 5).

- In Chapter 4, different techniques (SS-EPI, RS-EPI [1, 2], and DW-DESS [3]), were used and compared to visualize facial muscle fiber tracking. The RS-EPI seems to be a promising approach for visualization of muscle fiber orientation. And at the same time, the use of DW-DESS can provide additional information about small muscle groups due to its higher spatial resolution.

- In chapter 5, different diffusion models were elaborated to study the diffusion in renal pathologies in this retrospective study. The results were compared for the DWI signal in renal lesions and healthy volunteers. Besides mono-exponential model, quantification of renal DWI data by stretched-exponential model [4], diffusion kurtosis model [5] and bi-exponential model [6] can give additional parameters that enable a better characterization of different lesion types like cysts RCC, and AML.

6.2 Outlook

Future work will be focused on establishing the results in this thesis in a clinical environment, as well as further methodological developments.

- DTI and fiber tracking are promising tools that can bring a wealth of information about muscle structure and function. It is crucial to evaluate computationally the progressive changes in the facial muscle fibers due to CMF surgery. These changes cannot be tracked using histological methods. We hypothesize that using our results to reveal the specific muscle fiber changes after CMF surgery will provide direct assessment of the disorder's severity and sensitive measurement to predict clinical surgery outcome.

- The use of DWI data to extract the detailed micro structural features of tissues at the sub-voxel and even microscopic level continue to grow with improved hardware and better models. Although model dependent, these approaches may provide new features that should be of use in assessing development, degeneration, disease, and aging. The next step in this field of research would be to provide more accurate tumor detection and characterization with non-Gaussian diffusion models. Nevertheless, sensitivity, specificity and accuracy of the different models should be analyzed in further prospective studies, with including a large patient population.

In conclusion, the work that was done in this thesis was aimed to study the tissue micro-structure using DW MRI, with the potential to be directly useful for both basic research and clinics. Hopefully, my work will in the future be able to expand the knowledge and the possibility of diagnosis for different lesions, and improve the chances of patient recovery.

References

[1] S. J. Holdsworth, S. Skare, R. D. Newbould, R. Guzmann, N. H. Blevins, and R. Bammer, “Readout-segmented EPI for rapid high resolution diffusion imaging at 3 t,” *European journal of radiology*, vol. 65, pp. 36–46, Jan. 2008. 00000.

[2] D. A. Porter and R. M. Heidemann, “High resolution diffusion-weighted imaging using readout-segmented echo-planar imaging, parallel imaging and a two-dimensional navigator-based reacquisition,” *Magnetic Resonance in Medicine*, vol. 62, no. 2, p. 468–475, 2009. Cited by 0039.

[3] O. Bieri, C. Ganter, and K. Scheffler, “Quantitative in vivo diffusion imaging of cartilage using double echo steady-state free precession,” *Magnetic resonance in medicine: official journal of the Society of Magnetic Resonance in Medicine / Society of Magnetic Resonance in Medicine*, vol. 68, pp. 720–729, Sept. 2012. Cited by 0007.

[4] K. M. Bennett, K. M. Schmainda, R. T. Bennett, D. B. Rowe, H. Lu, and J. S. Hyde, “Characterization of continuously distributed cortical water diffusion rates with a stretched-exponential model,” *Magnetic resonance in medicine: official journal of the Society of Magnetic Resonance in Medicine / Society of Magnetic Resonance in Medicine*, vol. 50, pp. 727–734, Oct. 2003. Cited by 0096.

[5] J. H. Jensen, J. A. Helpern, A. Ramani, H. Lu, and K. Kaczynski, “Diffusional kurtosis imaging: the quantification of non-gaussian water diffusion by means of magnetic resonance imaging,” *Magnetic resonance in medicine: official journal of the Society of Magnetic Resonance in Medicine / Society of Magnetic Resonance in Medicine*, vol. 53, pp. 1432–1440, June 2005. Cited by 0292.

[6] D. Le Bihan, “Intravoxel incoherent motion perfusion MR imaging: a wake-up call,” *Radiology*, vol. 249, pp. 748–752, Dec. 2008. Cited by 0000.

Acknowledgment

I would never have been able to finish this thesis without the guidance of my supervisors, help from my friends, and support from my family.

I would like to express my sincerest gratitude to my advisor, Prof. Klaus Scheffler, for his guidance, caring, patience, and providing me with an excellent atmosphere for doing research. I would like to thank my supervisor, Markus Klarhöfer, who helps me with the research and practical issues beyond the textbooks, patiently corrected my writing and guiding my research during the past several years. Special thanks goes to Prof. Michael Bock, who was willing to participate in my final defense committee.

I would like to thank Franceso Santini, who as a good friend, was always willing to help and give his best suggestion. Many thanks to the present and former colleagues from radiological physics group of Basel and all my friends, especially Xenia and Claudia, for going through these years together. It would have been a lonely journey without all of you.

I would like to thank Gregor Sommor, a clinical collaborator, who always gives me help with the clinical study.

I would like to thank Chinese Scholarship Council, who financially supported my research for four years.

I would also like to thank my parents. They were always supporting me and encouraging me with their best wishes.

Curriculum Vitae

Personal Data

Name: Jinxia Zhu
Date of birth: 04 July 1983
Place of birth: Liaoning, China
Citizenship: Chinese
Address in Switzerland: Metzerstrasse 38, 4056 Basel

Education

Oct. 2009 - Dec. 2013: PhD in BioPhysics

University of Basel, Switzerland
Supervisor: Prof. Dr. Klaus Scheffler
Sept. Sept. 2006 - July 2009: MSc in Micro-electronics and Solid State Electronics
Dalian University of Technology, Dalian, China
Sept. 2002 - July 2006: Bachelor in Electronic Science and Technology
Dalian University of Technology, Dalian, China

Award

2009 4 Years Scholarship from Chinese Scholarship Council (CSC)